Research Square

Preprints are preliminary reports that have not undergone peer review.
They should not be considered conclusive, used to inform clinical practice,
or referenced by the media as validated information.

Monolithic solution and null-space condensation of internal variables in finite viscoelasticity

A. K.K. Sethuraman
University of Siegen
C. Hesch
christian.hesch@uni-siegen.de

University of Siegen

Research Article

Keywords: Finite-strain viscoelasticity, Internal-variable formulations, Newton methods, Schur-complement condensation, Null-space methods

Posted Date: April 19th, 2026

DOI: https://doi.org/10.21203/rs.3.rs-9245077/v1

License: This work is licensed under a Creative Commons Attribution 4.0 International License.
Read Full License

Additional Declarations: No competing interests reported.

Version of Record: A version of this preprint was published at Acta Mechanica on September 4th, 2026. See the published version at https://doi.org/10.1007/s00707-026-04891-3.

Monolithic solution and null-space condensation of internal variables in finite viscoelasticity.

A.K.K. Sethuraman, C. Hesch*

Chair of Computational Mechanics, University of Siegen, Siegen, Germany

Abstract

Finite-strain viscoelasticity is commonly discussed from a constitutive perspective, whereas the nonlinear solution architecture induced by time and space discretization is studied less systematically. In this work, we consider a representative viscoelastic model with a strain-like internal variable and focus on the fully discrete coupled problem in the deformation and the internal state. Starting from the underlying energy–dissipation structure, we derive the discrete weak forms and obtain a monolithic Newton system with a naturally non-symmetric block tangent. The increment of the internal variable is eliminated consistently at the level of the linearized system by a Schur complement, and the same reduction is shown to admit a geometric interpretation in terms of a null-space basis of the tangent space of the internal constraint manifold. This yields a genuinely monolithic counterpart to classical nested Gauss-point condensation, in which local constitutive equations are solved separately before the global equilibrium step. Numerical results for two- and three-dimensional Cook's membrane benchmarks show that the proposed strategy retains essentially the same outer Newton behavior as the classical approach while substantially reducing computational cost by avoiding repeated local Newton solves; it also remains convergent for load increments for which the nested scheme fails. Moreover, the numerical study suggests that suitably chosen approximation spaces for the internal variable can yield additional savings in computational effort without significant loss of accuracy. Although presented for finite viscoelasticity, the construction extends naturally to broader classes of thermodynamically consistent internal-variable models.

Keywords: Finite-strain viscoelasticity; Internal-variable formulations; Newton methods; Schur-complement condensation; Null-space methods

*Corresponding author. E-mail address: christian.hesch@uni-siegen.de

1 Introduction

Finite-strain viscoelasticity has given rise to a broad range of constitutive models over the past decades [17, 26, 13, 24, 2]. A large part of the literature is driven by thermodynamic admissibility, constitutive flexibility, and the ability to reproduce experimental data [15, 1, 19, 18, 14, 12]. From this perspective, the main emphasis is typically placed on the choice of free energy, on the formulation of the internal evolution law, and on the calibration of material parameters. Compared with the broad constitutive literature, the nonlinear solution architecture has received less systematic attention; representative contributions include [8, 3, 22, 6, 25, 16].

From a numerical point of view, however, this solution architecture is of central importance. After temporal and spatial discretization, finite viscoelasticity with internal variables leads to a coupled nonlinear algebraic system in the deformation and the internal state. In many implementations, the evolution equations for the internal variables are treated as local constitutive updates and are solved by nested Newton iterations at the quadrature-point level, [8]. While this classical viewpoint is natural from the material-modeling side, it tends to hide the structure of the fully discrete problem and may lead to considerable computational overhead due to repeated local solves. Moreover, the interaction between the global equilibrium iterations, the local constitutive iterations, and the approximation space chosen for the internal variables is rarely studied systematically.

In the present contribution, we deliberately take the opposite viewpoint. We use a finite viscoelastic model with a strain-like internal variable $\boldsymbol{C}_i$ as a representative test bed, but our primary interest is not the proposal of yet another constitutive law. Instead, we focus on the common algorithmic structure shared by a broader class of thermodynamically consistent internal-variable models [7, 23, 4, 20, 21]. The essential ingredients are a free energy, a local evolution equation (or, more generally, a set of internal constraints), and the availability of a consistent tangent for the internal residual. Once these ingredients are available, the coupled problem can be formulated and solved monolithically at the fully discrete level.

Starting from the underlying energy-dissipation structure of the continuum model, we derive weak forms of the balance of linear momentum and of the internal evolution equation and discretize them in time by a midpoint rule. This leads to a single nonlinear system in the deformation and the internal variable field. Its Newton linearization has a natural block structure and, in general, a non-symmetric tangent matrix. Based on this structure, the increment of the internal variable can be condensed systematically by a Schur complement. At the same time, the same reduction admits a geometric interpretation through a null-space basis of the tangent space of the internal constraint manifold. Related monolithic reduction ideas have already been shown to be effective in other nonlinear mechanics settings, such as computational homogenization [10], overlapping domain decomposition [11], and higher-order patch-coupling procedures [5]. These results motivate the present transfer of the methodology to finite viscoelasticity.

This viewpoint also clarifies the distinction between the proposed monolithic strategy and the classical nested Gauss-point condensation. In the classical setting, the internal evolution equation is solved locally and nonlinearly before the global equilibrium problem is assembled. In the monolithic setting pursued here, the internal residual remains part of the global Newton process and is condensed only at the level of the linearized system.

Algebraically, both approaches are closely related, but algorithmically the difference is substantial: the monolithic formulation avoids repeated local Newton solves and retains the effect of non-vanishing internal residuals during the global iterations.

The aim of this paper is therefore twofold. First, we formulate a monolithic solution framework for finite viscoelasticity with a strain-like internal variable and show how the internal equations can be condensed consistently at the level of the fully discrete Newton system, both algebraically and geometrically. Second, we assess the computational consequences of this formulation in representative benchmark problems. To this end, we compare the proposed monolithic strategy with a classical nested condensation scheme in two- and three-dimensional Cook's membrane examples and study how different approximation spaces for the internal variable affect accuracy, computational cost, and nonlinear robustness.

Although the numerical examples are restricted to finite viscoelasticity, the construction itself is not tied to one particular viscosity law. Rather, it reflects a fully discrete solver structure that is relevant for a broader class of thermodynamically consistent internal-variable models, including generalized standard materials and viscoplastic regularizations of finite-strain plasticity. In this sense, the present work is intended as a contribution to nonlinear computational mechanics as much as to finite viscoelasticity itself.

Section 1.1 summarizes the notation used throughout the paper. Section 2 introduces the continuum model and its thermodynamic structure. Section 3 derives the weak forms and the midpoint time discretization. Section 4 presents the monolithic Newton system together with the Schur-complement and null-space condensation of the internal variable. Finally, Section 5 discusses the numerical examples.

1.1 Definitions and notations.

This section summarizes the notation used throughout the paper. A contraction of two vectors will be understood as $[\boldsymbol{a}\cdot\boldsymbol{b}] = a_i\, b_i$, where the Einstein summation convention on repeated indices is used. For two second order tensors it holds $[\boldsymbol{A}\,\boldsymbol{B}]_{ij} = A_{ik}\, B_{kj}$ and the double contraction reads $[\boldsymbol{A} : \boldsymbol{B}] = A_{ij}\, B_{ij}$. Next, we define the gradient with respect to the reference $\nabla_X(\bullet)$ of a vector field $\boldsymbol{a}$ and of a second-order tensor field $\boldsymbol{A}$ as

$$[\nabla_X(\boldsymbol{a})]_{iJ} = \frac{\partial a_i}{\partial X_J}, \qquad [\nabla_X(\boldsymbol{A})]_{iJK} = \frac{\partial A_{iJ}}{\partial X_K}. \tag{1}$$

For the divergence operator it follows

$$[\nabla_X \cdot \boldsymbol{A}]_i = \frac{\partial A_{iJ}}{\partial X_J}, \qquad [\nabla_X \cdot \mathfrak{A}]_{iJ} = \frac{\partial \mathfrak{A}_{iJK}}{\partial X_K}. \tag{2}$$

We work in a three-dimensional reference configuration $\mathcal{B}_0 \subset \mathbb{R}^3$. Second-order tensors are elements of $\mathbb{R}^{3\times3}$. We denote by

$$\mathrm{S}^3 := \left\{ \boldsymbol{A} \in \mathbb{R}^{3\times3} \,\middle|\, \boldsymbol{A} = \boldsymbol{A}^{\mathsf{T}} \right\} \qquad \text{and} \qquad \mathrm{S}^+ := \left\{ \boldsymbol{A} \in \mathrm{S}^3 \,\middle|\, \boldsymbol{A} \text{ is positive definite} \right\} \tag{3}$$

the space of symmetric and the open cone of symmetric positive-definite second-order tensors, respectively. Whenever we write $\boldsymbol{A} : \mathcal{B}_0 \to \mathrm{S}^+$, this means that for each material point $\boldsymbol{X} \in \mathcal{B}_0$ the value $\boldsymbol{A}(\boldsymbol{X}, t)$ is a symmetric positive-definite 3×3 tensor.

2 Preliminaries and problem description

We start with a short summary of nonlinear continuum mechanics. In particular, we aim at finite viscoelasticity with a strain-like internal variable, considered as additional field defined on its reference configuration as bounded Lipschitz domain $\mathcal{B}_0 \subset \mathbb{R}^3$ with boundary $\partial\mathcal{B}_0$ and outward unit normal $\boldsymbol{N}$. The actual configuration $\mathcal{B} \subset \mathbb{R}^3$ with boundary $\partial\mathcal{B}$ and outward unit normal $\boldsymbol{n}$ is related to the reference configuration by a deformation mapping $\boldsymbol{\varphi} : \mathcal{B}_0 \to \mathbb{R}^3$, such that $\mathcal{B} = \boldsymbol{\varphi}(\mathcal{B}_0)$. Material points are labelled by $\boldsymbol{X} \in \mathcal{B}_0$ with corresponding actual position $\boldsymbol{x} = \boldsymbol{\varphi}(\boldsymbol{X})$.

We formulate the continuum model in three spatial dimensions, $\mathcal{B}_0 \subset \mathbb{R}^3$, but the structure carries over verbatim to two-dimensional settings ($d = 2$), e.g. plane-strain problems, as will be shown in the examples.

2.1 Kinematics and internal variable

Within nonlinear continuum mechanics, the deformation gradient is a second-order tensor field, described by

$$\boldsymbol{F} : \mathcal{B}_0 \times [0,T] \to \mathbb{R}^{3\times 3},\ \boldsymbol{F} = \nabla_X(\boldsymbol{\varphi}),$$

and the right Cauchy–Green tensor is given by $\boldsymbol{C} : \mathcal{B}_0 \times [0,T] \to \mathrm{S}^+,\ \boldsymbol{C} = \boldsymbol{F}^{\mathrm{T}}\boldsymbol{F}$. Moreover, the internal variable field is given by

$$\boldsymbol{C}_i : \mathcal{B}_0 \times [0,T] \to \mathrm{S}^+ .$$

Viscous deformation is often described by an internal deformation gradient $\boldsymbol{F}_i$ via the formal multiplicative split

$$\boldsymbol{F} = \boldsymbol{F}_e\boldsymbol{F}_i,$$

where $\boldsymbol{F}_e$ denotes the elastic part and $\boldsymbol{F}_i$ the inelastic (viscous) part. This motivates the internal strain-like variable

$$\boldsymbol{C}_i = \boldsymbol{F}_i^{\mathrm{T}}\boldsymbol{F}_i \in \mathrm{S}^+,$$

and the elastic right Cauchy–Green tensor

$$\boldsymbol{F}_e^{\mathrm{T}}\boldsymbol{F}_e = \boldsymbol{F}_i^{-\mathrm{T}}\,\boldsymbol{C}\,\boldsymbol{F}_i^{-1}.$$

For the variationally consistent framework it is more convenient to work with the elastic strain measure $\boldsymbol{C}_e$ in the reference configuration

$$\boldsymbol{C}_e = \boldsymbol{C}\,\boldsymbol{C}_i^{-1},$$

which lives entirely in the reference configuration and has the same invariants as $\boldsymbol{F}_e^{\mathrm{T}}\boldsymbol{F}_e$ in the isotropic case.

2.2 Free energy, stresses and driving forces

The specific Helmholtz free energy per reference volume is additively split into an equilibrium part and a non-equilibrium part:

$$\Psi(\boldsymbol{C}, \boldsymbol{C}_i) = \Psi_{\mathrm{eq}}(\boldsymbol{C}) + \Psi_{\mathrm{neq}}(\boldsymbol{C}_e), \tag{4}$$

where we assume isotropy so that both parts depend only on the invariants of their arguments (cf. [24], [6]).

The second Piola–Kirchhoff stress follows from the usual constitutive relation

$$\boldsymbol{S} = 2\,\frac{\partial \Psi}{\partial \boldsymbol{C}} = \boldsymbol{S}_{\mathrm{eq}} + \boldsymbol{S}_{\mathrm{neq}}.$$

By the chain rule applied to (4),

$$\boldsymbol{S}_{\mathrm{eq}} = 2\,\frac{\partial \Psi_{\mathrm{eq}}}{\partial \boldsymbol{C}}, \tag{5}$$

$$\boldsymbol{S}_{\mathrm{neq}} = 2\,\frac{\partial \Psi_{\mathrm{neq}}}{\partial \boldsymbol{C}_e} \,:\, \frac{\partial \boldsymbol{C}_e}{\partial \boldsymbol{C}} = 2\,\frac{\partial \Psi_{\mathrm{neq}}}{\partial \boldsymbol{C}_e}\,\boldsymbol{C}_i^{-1}, \tag{6}$$

since $\partial \boldsymbol{C}_e / \partial \boldsymbol{C} = \boldsymbol{I} \boxtimes \boldsymbol{C}_i^{-1}$. It is convenient to introduce the mixed thermodynamic driving force associated with the non-equilibrium part

$$\boldsymbol{M} = \boldsymbol{S}_{\mathrm{neq}}\,\boldsymbol{C} = 2\,\frac{\partial \Psi_{\mathrm{neq}}}{\partial \boldsymbol{C}_e}\,\boldsymbol{C}_i^{-1}\,\boldsymbol{C}, \tag{7}$$

which will play the role of thermodynamic driving force for the viscous evolution. Using the chain rule, it is straightforward to rewrite the thermodynamic driving force as

$$\boldsymbol{M} = -2\,\frac{\partial \Psi_{\mathrm{neq}}}{\partial \boldsymbol{C}_i}\,\boldsymbol{C}_i, \tag{8}$$

where the minus sign stems from the appearance of $\boldsymbol{C}_i$ in $\boldsymbol{C}_e = \boldsymbol{C}\boldsymbol{C}_i^{-1}$ and is absorbed in their definition of the non-equilibrium stress. Note that $\boldsymbol{M}$ is in general not symmetric and according to [6], is an isotropic tensor function in a linear space $\mathbb{L}(T^*_X\mathcal{B}_0, T^*_X\mathcal{B}_0)$.

2.3 Clausius–Duhem inequality and conjugate pair $(\boldsymbol{M}, \boldsymbol{L}_i)$

In Lagrangian form the Clausius–Duhem inequality reads

$$\mathcal{D}_{\mathrm{int}} = \boldsymbol{S} : \tfrac{1}{2}\dot{\boldsymbol{C}} - \dot{\Psi}(\boldsymbol{C}, \boldsymbol{C}_i) \;\geq 0. \tag{9}$$

Using (4),

$$\dot{\Psi} = \frac{\partial \Psi_{\mathrm{eq}}}{\partial \boldsymbol{C}} : \dot{\boldsymbol{C}} + \frac{\partial \Psi_{\mathrm{neq}}}{\partial \boldsymbol{C}_e} : \dot{\boldsymbol{C}}_e,$$

where the elastic strain measure evolves according to

$$\dot{\boldsymbol{C}}_e = \dot{\boldsymbol{C}}\,\boldsymbol{C}_i^{-1} + \boldsymbol{C}\,\frac{\mathrm{d}}{\mathrm{d}t}(\boldsymbol{C}_i^{-1}).$$

Using the standard relation

$$\frac{\mathrm{d}}{\mathrm{d}t}(\boldsymbol{C}_i^{-1}) = -\,\boldsymbol{C}_i^{-1}\dot{\boldsymbol{C}}_i\,\boldsymbol{C}_i^{-1},$$

we obtain

$$\dot{\boldsymbol{C}}_e = \dot{\boldsymbol{C}}\,\boldsymbol{C}_i^{-1} - \boldsymbol{C}\,\boldsymbol{C}_i^{-1}\dot{\boldsymbol{C}}_i\,\boldsymbol{C}_i^{-1}.$$

Substituting into (9) and exploiting $\boldsymbol{S}_{\mathrm{eq}} = 2\,\partial\Psi_{\mathrm{eq}}/\partial\boldsymbol{C}$ yields

$$\begin{aligned}\mathcal{D}_{\mathrm{int}} &= \boldsymbol{S}_{\mathrm{neq}} : \tfrac{1}{2}\dot{\boldsymbol{C}} - \frac{\partial\Psi_{\mathrm{neq}}}{\partial\boldsymbol{C}_e} : \left(\dot{\boldsymbol{C}}\,\boldsymbol{C}_i^{-1} - \boldsymbol{C}\,\boldsymbol{C}_i^{-1}\dot{\boldsymbol{C}}_i\,\boldsymbol{C}_i^{-1}\right)\\ &= \left(\boldsymbol{S}_{\mathrm{neq}} : \tfrac{1}{2}\dot{\boldsymbol{C}} - \frac{\partial\Psi_{\mathrm{neq}}}{\partial\boldsymbol{C}_e} : \dot{\boldsymbol{C}}\,\boldsymbol{C}_i^{-1}\right) + \frac{\partial\Psi_{\mathrm{neq}}}{\partial\boldsymbol{C}_e} : \boldsymbol{C}\,\boldsymbol{C}_i^{-1}\dot{\boldsymbol{C}}_i\,\boldsymbol{C}_i^{-1}. \qquad (10)\end{aligned}$$

The first bracket only contains elastic rates and cancels out for the usual choice of the free energy (details in [24]). The remaining purely viscous contribution can be written as

$$\mathcal{D}_{\mathrm{int}} = \boldsymbol{M} : \boldsymbol{L}_i^T, \qquad (11)$$

where $\boldsymbol{L}_i = \frac{1}{2}\boldsymbol{C}_i^{-1}\dot{\boldsymbol{C}}_i$ is a rate-of-deformation tensor again in the linear space $\mathbb{L}(T_X\mathcal{B}_0, T_X\mathcal{B}_0)$ associated with the internal process, i.e. a suitable material representation of the internal velocity gradient. In other words, the dissipation density is the power-conjugate product of driving force $\boldsymbol{M}$ and flux $\boldsymbol{L}_i$. This can be, regarding eq. (8), rewritten as

$$\mathcal{D}_{\mathrm{int}} = -\frac{\partial\Psi_{\mathrm{neq}}}{\partial\boldsymbol{C}_i} : \dot{\boldsymbol{C}}_i.$$

Equation (11) is the key outcome of thermodynamics: the internal variable enters the Clausius–Duhem inequality only through the pair $(\boldsymbol{M}, \boldsymbol{L}_i)$, and any constitutive choice must ensure $\mathcal{D}_{\mathrm{int}} \geq 0$.

Remark 1. *Although $\boldsymbol{C}_i$ and $\dot{\boldsymbol{C}}_i$ are symmetric, the associated viscous deformation rate $\boldsymbol{L}_i := \frac{1}{2}\,\boldsymbol{C}_i^{-1}\dot{\boldsymbol{C}}_i$ is in general not symmetric. Hence $\boldsymbol{L}_i$ (and $\boldsymbol{M}$) are to be interpreted as mixed tensors. If symmetry is required for the thermodynamics driving force, one could use*

$$\boldsymbol{\Sigma} := -\frac{\partial\Psi_{\mathrm{neq}}}{\partial\boldsymbol{C}_i} = \frac{1}{2}\,\boldsymbol{M}\,\boldsymbol{C}_i^{-1}, \quad \boldsymbol{\Sigma} \in \mathrm{S}^3,$$

instead of the thermodynamic driving force from the non-equilibrium part.

2.4 Variational structure and evolution law

We now use (11) to define a constitutive relation between the thermodynamic driving force $\boldsymbol{M}$ and the viscous rate $\boldsymbol{L}_i$. This relation is chosen such that it arises from a local variational principle and automatically satisfies the dissipation inequality.

2.4.1 Linear viscous law and positivity

A natural and widely used choice is a linear relation of the form

$$\boldsymbol{M} = \mathbb{V} : \boldsymbol{L}_i^T, \tag{12}$$

where $\mathbb{V}$ is a fourth-order viscosity tensor. For isotropic materials we use the usual volumetric–deviatoric split

$$\mathbb{V} = V_{\mathrm{vol}}\,\mathbb{P}_{\mathrm{vol}} + 2V_{\mathrm{dev}}\,\mathbb{P}_{\mathrm{dev}}, \qquad V_{\mathrm{vol}} > 0,\ V_{\mathrm{dev}} > 0, \tag{13}$$

where $\mathbb{P}_{\mathrm{vol}} : \boldsymbol{A} = \mathrm{vol}(\boldsymbol{A})$, $\mathrm{vol}(\boldsymbol{A}) = \frac{1}{d}\,\mathrm{tr}(\boldsymbol{A})\boldsymbol{I}$ and $\mathbb{P}_{\mathrm{dev}} : \boldsymbol{A} = \mathrm{dev}(\boldsymbol{A})$, $\mathrm{dev}(\boldsymbol{A}) = \boldsymbol{A} - \mathrm{vol}(\boldsymbol{A})$. Inserting (12) into (11) gives

$$\mathcal{D}_{\mathrm{int}} = \boldsymbol{M} : \boldsymbol{L}_i^T = \boldsymbol{L}_i^T : \mathbb{V} : \boldsymbol{L}_i^T \ \geq 0, \tag{14}$$

because $\mathbb{V}$ is positive semidefinite if $V_{\mathrm{vol}}, V_{\mathrm{dev}} \geq 0$. This guarantees that the Clausius–Duhem inequality is satisfied in the continuum. In this form, the evolution law is simply the constitutive equation (12). It prescribes the stress-like variable $\boldsymbol{M}$ in terms of the rate $\boldsymbol{L}_i$.

2.4.2 Maximum dissipation principle

The same law can be obtained from a local variational principle, which makes the generalized standard-material structure explicit. We start from the quadratic dissipation potential in the rate $\boldsymbol{L}_i$,

$$\Phi(\boldsymbol{L}_i) = \tfrac{1}{2}\,\boldsymbol{L}_i : \mathbb{V} : \boldsymbol{L}_i. \tag{15}$$

With this at hand, a variational principle can be formulated by introducing

$$\mathcal{J}(\boldsymbol{L}_i) := \boldsymbol{M} : \boldsymbol{L}_i^T - \Phi(\boldsymbol{L}_i) = \boldsymbol{M} : \boldsymbol{L}_i^T - \tfrac{1}{2}\,\boldsymbol{L}_i : \mathbb{V} : \boldsymbol{L}_i. \tag{16}$$

As $\Phi(\boldsymbol{L}_i)$ is convex, the functional $\mathcal{J}$ is concave in $\boldsymbol{L}_i$, and the physically realized rate is obtained as

$$\boldsymbol{L}_i = \arg\sup_{\boldsymbol{L}_i} \mathcal{J}(\boldsymbol{L}_i).$$

and we obtain

$$\delta\mathcal{J} = \Big(\boldsymbol{M}^T - \mathbb{V} : \boldsymbol{L}_i\Big) : \delta\boldsymbol{L}_i = 0 \quad \forall\,\delta\boldsymbol{L}_i, \tag{17}$$

evaluated for a fixed $\boldsymbol{M}$. Note, that the constitutive evolution equation cannot be derived as part of a Ritz formalism; however, we can always multiply (12) with an appropriate test function $\delta\boldsymbol{L}_i$.

In the following we assume that the viscosity tensor $\mathbb{V}$ is invertible. With this, the associated complementary (Legendre-dual) dissipation potential in the driving force $\boldsymbol{M}$ is

$$\Phi^*(\boldsymbol{M}) := \sup_{\boldsymbol{L}_i}\Big(\boldsymbol{M} : \boldsymbol{L}_i^T - \Phi(\boldsymbol{L}_i)\Big) \tag{18}$$

$$= \Big[\boldsymbol{M} : \boldsymbol{L}_i^T - \tfrac{1}{2}\,\boldsymbol{L}_i : \mathbb{V} : \boldsymbol{L}_i\Big]_{\boldsymbol{L}_i = \mathbb{V}^{-1} : \boldsymbol{M}^T} = \tfrac{1}{2}\,\boldsymbol{M} : \mathbb{V}^{-1} : \boldsymbol{M}. \tag{19}$$

where $\mathbb{V}^{-1}$ denotes the inverse of the fourth-order tensor $\mathbb{V}$. Using Φ^*, the principle of maximum dissipation can be formulated as follows: for a given viscous rate $\boldsymbol{L}_i$, the physically realized thermodynamic driving force $\boldsymbol{M}$ maximizes

$$\mathcal{J}^*(\boldsymbol{M};\boldsymbol{L}_i) := \boldsymbol{M} : \boldsymbol{L}_i^T - \Phi^*(\boldsymbol{M}) = \boldsymbol{M} : \boldsymbol{L}_i^T - \tfrac{1}{2}\,\boldsymbol{M} : \mathbb{V}^{-1} : \boldsymbol{M} \tag{20}$$

with respect to $\boldsymbol{M}$ and a fixed $\boldsymbol{L}_i$. Hence, stationarity with regard to $\boldsymbol{M}$ gives

$$\delta\mathcal{J}^* = \Big(\boldsymbol{L}_i^T - \mathbb{V}^{-1} : \boldsymbol{M}\Big) : \delta\boldsymbol{M} = 0 \quad \forall\,\delta\boldsymbol{M}, \tag{21}$$

and thus

$$\boldsymbol{L}_i = \Big(\mathbb{V}^{-1} : \boldsymbol{M}\Big)^T, \tag{22}$$

which is again the linear viscous law presented in (12). The maximum property follows from the strict convexity of Φ^*, with regard to the positive definiteness of $\mathbb{V}$. In this dual formulation, the evolution law appears as the Euler equation of a local variational problem in $\boldsymbol{M}$: among all admissible driving forces $\boldsymbol{M}$ it selects the one that maximizes the dissipation functional $\mathcal{J}^*(\boldsymbol{M};\boldsymbol{L}_i)$ for the given rate $\boldsymbol{L}_i$.

As we have a linear relation between the driving force $\boldsymbol{M}$ and the rate $\dot{\boldsymbol{C}}_i$, we can solve for $\dot{\boldsymbol{C}}_i$ using

$$\dot{\boldsymbol{C}}_i := 2\,\boldsymbol{C}_i\Big(\mathbb{V}^{-1} : \boldsymbol{M}(\boldsymbol{C},\boldsymbol{C}_i)\Big)^T. \tag{23}$$

and we obtain

$$\Big(\dot{\boldsymbol{C}}_i - 2\,\boldsymbol{C}_i(\mathbb{V}^{-1} : \boldsymbol{M})^T\Big) : \delta\boldsymbol{\Sigma} = 0 \quad \forall\,\delta\boldsymbol{\Sigma} \quad \text{with} \quad \delta\boldsymbol{\Sigma} \in \mathrm{S}^3\,. \tag{24}$$

In the vicinity of thermodynamic equilibrium ($\boldsymbol{C}_e \approx \boldsymbol{I}$), a standard linearization of (23) yields the familiar finite linear viscoelastic relation

$$\dot{\boldsymbol{C}}_i \approx \frac{1}{\tau}\Big(\boldsymbol{C} - \boldsymbol{C}_i\Big), \tag{25}$$

with an effective relaxation time τ; see [24] for details in the small-deviation regime.

2.5 Global energy functional and dissipation balance

We consider a body $\mathcal{B}_0 \subset \mathbb{R}^3$ in the reference configuration with mass density $\rho_0(\boldsymbol{X})$ and motion $\boldsymbol{\varphi}(\boldsymbol{X},t)$. The Lagrangian velocity is $\boldsymbol{v} := \dot{\boldsymbol{\varphi}}$. The kinetic energy reads

$$E_{\mathrm{kin}}(t) = \frac{1}{2}\int_{\mathcal{B}_0} \rho_0(\boldsymbol{X})\,\boldsymbol{v}(\boldsymbol{X},t)\cdot\boldsymbol{v}(\boldsymbol{X},t)\,\mathrm{d}V. \tag{26}$$

The stored (Helmholtz) free energy of the viscoelastic material is obtained by spatial integration of the local density $\Psi(\boldsymbol{C},\boldsymbol{C}_i)$,

$$U_{\mathrm{int}}(t) := \int_{\mathcal{B}_0} \Psi\Big(\boldsymbol{C}(\boldsymbol{X},t),\boldsymbol{C}_i(\boldsymbol{X},t)\Big)\,\mathrm{d}V, \tag{27}$$

and, by definition, we obtain

$$\dot{U}_{\mathrm{int}}(t) = \int_{\mathcal{B}_0} \dot{\Psi}(\boldsymbol{C},\boldsymbol{C}_i)\,\mathrm{d}V. \tag{28}$$

The local Clausius–Duhem inequality (9) yields the global internal dissipation

$$D_{\mathrm{int}}(t) := \int_{\mathcal{B}_0} \mathcal{D}_{\mathrm{int}}\,\mathrm{d}V = \int_{\mathcal{B}_0} \boldsymbol{S} : \tfrac{1}{2}\dot{\boldsymbol{C}}\,\mathrm{d}V - \dot{U}_{\mathrm{int}}(t) \;\geq 0, \tag{29}$$

or equivalently, using (11),

$$D_{\mathrm{int}}(t) = \int_{\mathcal{B}_0} \boldsymbol{M}(\boldsymbol{X},t) : \boldsymbol{L}_i^T(\boldsymbol{X},t)\,\mathrm{d}V \;\geq 0. \tag{30}$$

The internal mechanical power is given by

$$P_{\mathrm{int}}(t) := \int_{\mathcal{B}_0} \boldsymbol{S} : \tfrac{1}{2}\dot{\boldsymbol{C}}\,\mathrm{d}V, \tag{31}$$

such that (29) can be written in compact form

$$\dot{U}_{\mathrm{int}}(t) = P_{\mathrm{int}}(t) - D_{\mathrm{int}}(t), \qquad D_{\mathrm{int}}(t) \geq 0. \tag{32}$$

Let the boundary of $\mathcal{B}_0$ be decomposed into a Dirichlet part $\partial\mathcal{B}_0^u$ and a Neumann part $\partial\mathcal{B}_0^t$, and let $\boldsymbol{b}_0(\boldsymbol{X},t)$ and $\boldsymbol{t}_0(\boldsymbol{X},t)$ denote prescribed body forces and tractions (per reference volume and per reference area, respectively). The external mechanical power is

$$P_{\mathrm{ext}}(t) := \int_{\mathcal{B}_0} \rho_0\,\boldsymbol{b}_0 \cdot \boldsymbol{v}\,\mathrm{d}V + \int_{\partial\mathcal{B}_0^t} \boldsymbol{t}_0 \cdot \boldsymbol{v}\,\mathrm{d}A. \tag{33}$$

The balance of linear momentum, multiplied by $\boldsymbol{v}$ and integrated over $\mathcal{B}_0$, yields the global mechanical power balance

$$\dot{E}_{\mathrm{kin}}(t) + P_{\mathrm{int}}(t) = P_{\mathrm{ext}}(t). \tag{34}$$

Combining (32) and (34) leads to the global energy balance

$$\frac{\mathrm{d}}{\mathrm{d}t}\Big(E_{\mathrm{kin}}(t) + U_{\mathrm{int}}(t)\Big) = P_{\mathrm{ext}}(t) - D_{\mathrm{int}}(t), \qquad D_{\mathrm{int}}(t) \geq 0. \tag{35}$$

If all external loads are conservative, $P_{\mathrm{ext}}(t)$ can be written as the negative time derivative of an external potential $U_{\mathrm{ext}}(t)$, and the total mechanical energy

$$\mathcal{V}(t) := E_{\mathrm{kin}}(t) + U_{\mathrm{int}}(t) + U_{\mathrm{ext}}(t) \tag{36}$$

satisfies

$$\dot{\mathcal{V}}(t) = -\,D_{\mathrm{int}}(t) \;\leq 0. \tag{37}$$

Thus, the continuous formulation automatically complies with the second law of thermodynamics: the total energy can only decay by the amount of viscous dissipation. In the fully discrete setting the midpoint discretization is designed to mimic the underlying energy–dissipation structure as closely as possible, see [6] for the algorithmic enforcement of the energy balance in the discrete setting. At this point, the continuous thermodynamic structure of the model is completely specified by the free energy $\Psi(\boldsymbol{C},\boldsymbol{C}_i)$, the Clausius–Duhem inequality (9) and the evolution law for $\boldsymbol{C}_i$.

3 Integral weak forms and midpoint time discretization

Starting from the global energy and power balances derived above, we now introduce weak forms of the momentum balance and of the evolution equation on $\mathcal{B}_0$. These will be discretized in time by a midpoint rule in order to obtain a fully discrete system that preserves the underlying energy–dissipation structure as closely as possible.

3.1 Weak form of the momentum balance

We now elaborate the problem described in (37) in detail. Starting from the balance of linear momentum in the reference configuration, multiplication by an admissible virtual displacement and integration over $\mathcal{B}_0$ yields the weak form: Find $\boldsymbol{\varphi}(t)$ with $\boldsymbol{\varphi}(t) = \bar{\boldsymbol{\varphi}}(t)$ on $\partial\mathcal{B}_0^{\mathrm{D}}$ and $\delta\boldsymbol{\varphi}(t) = \mathbf{0}$ on $\partial\mathcal{B}_0^{\mathrm{D}}$, such that for all admissible test functions $\delta\boldsymbol{\varphi}$ with

$$\int_{\mathcal{B}_0} \rho_0\, \delta\boldsymbol{\varphi} \cdot \ddot{\boldsymbol{\varphi}}\, \mathrm{d}V + \int_{\mathcal{B}_0} \boldsymbol{P}(\boldsymbol{C}, \boldsymbol{C}_i) : \nabla_X(\delta\boldsymbol{\varphi})\, \mathrm{d}V = \int_{\mathcal{B}_0} \rho_0\, \boldsymbol{b}_0 \cdot \delta\boldsymbol{\varphi}\, \mathrm{d}V + \int_{\partial\mathcal{B}_0^{\mathrm{N}}} \bar{\boldsymbol{t}}_0 \cdot \delta\boldsymbol{\varphi}\, \mathrm{d}A. \quad (38)$$

Here $\boldsymbol{P}$ is the first Piola–Kirchhoff stress induced by the second Piola–Kirchhoff stress $\boldsymbol{S}(\boldsymbol{C}, \boldsymbol{C}_i)$ from Section 2.2, i.e. $\boldsymbol{P} = \boldsymbol{F}\,\boldsymbol{S}$. Using standard arguments in variational calculus, we end up with the local balance of linear momentum in the reference configuration

$$\mathrm{Div}_X\, \boldsymbol{P}(\boldsymbol{C}, \boldsymbol{C}_i) + \rho_0\, \boldsymbol{b}_0(\boldsymbol{X}, t) = \rho_0\, \ddot{\boldsymbol{\varphi}}(\boldsymbol{X}, t) \quad \text{in } \mathcal{B}_0,$$

with prescribed tractions $\bar{\boldsymbol{t}}_0$ on $\partial\mathcal{B}_0^{\mathrm{N}}$ and prescribed motion $\bar{\boldsymbol{\varphi}}$ on $\partial\mathcal{B}_0^{\mathrm{D}}$. Note that this local form allows us to elaborate the explicit structure of the boundary conditions in detail, which is a non-trivial task for, e.g., higher order materials.

For the integral evolution equation and global maximum dissipation, a purely material weak form of the stationarity condition in (24) is obtained by testing the residual with an arbitrary symmetric tensor field $\delta\boldsymbol{\Sigma} : \mathcal{B}_0 \to \mathrm{S}^3$,

$$\int_{\mathcal{B}_0} \delta\boldsymbol{\Sigma} : \left(\dot{\boldsymbol{C}}_i - 2\,\boldsymbol{C}_i \mathbb{V}^{-1} : \boldsymbol{M}^T\right) \mathrm{d}V = 0. \quad (39)$$

Alternatively, we may use $\delta\boldsymbol{C}_i : \mathcal{B}_0 \to \mathrm{S}^3$ following the formulation presented in (17). In a classical setting, using the evolution equation as internal ODE at each quadrature point, this choice is arbitrary. However, in the variational setting presented here, a careful evaluation is necessary.

3.2 Temporal discretisation

For the time-discrete problem we consider two consecutive time levels t_n and t_{n+1} with step size $h = t_{n+1} - t_n$. Let

$$\boldsymbol{v} := \dot{\boldsymbol{\varphi}}, \qquad \boldsymbol{v}^n := \boldsymbol{v}(\cdot, t_n), \quad \boldsymbol{v}^{n+1} := \boldsymbol{v}(\cdot, t_{n+1}),$$

and introduce midpoint quantities by

$$(\bullet)_{n+\frac{1}{2}} := \tfrac{1}{2}\left((\bullet)^{n+1} + (\bullet)^n\right), \qquad \boldsymbol{v}_{n+\frac{1}{2}} := \frac{\boldsymbol{\varphi}^{n+1} - \boldsymbol{\varphi}^n}{h}, \quad \boldsymbol{a}_{n+\frac{1}{2}} := \frac{\boldsymbol{v}^{n+1} - \boldsymbol{v}^n}{h},$$

such that

$$\boldsymbol{\varphi}^{n+1} - \boldsymbol{\varphi}^{n} = \frac{h}{2}(\boldsymbol{v}^{n+1} + \boldsymbol{v}^{n}),$$

providing a direct relationship between $\boldsymbol{\varphi}^{n+1}$ and $\boldsymbol{v}^{n+1}$ for given values at time $t = t_n$. Next, we introduce midpoint kinematic and material quantities

$$\boldsymbol{C}_{n+\frac{1}{2}} := \boldsymbol{F}_{n+\frac{1}{2}}^{\mathsf{T}} \boldsymbol{F}_{n+\frac{1}{2}}, \qquad \boldsymbol{C}_{i,n+\frac{1}{2}} := \tfrac{1}{2}(\boldsymbol{C}_i^{n+1} + \boldsymbol{C}_i^{n}),$$

with $\boldsymbol{F}_{n+\frac{1}{2}} := \nabla_X(\boldsymbol{\varphi}_{n+\frac{1}{2}})$ and $\boldsymbol{C}_{e,n+\frac{1}{2}} := \boldsymbol{C}_{n+\frac{1}{2}}\, \boldsymbol{C}_{i,n+\frac{1}{2}}^{-1}$. The first Piola–Kirchhoff stress at the midpoint is then

$$\boldsymbol{P}_{n+\frac{1}{2}} := \boldsymbol{P}\Big(\boldsymbol{C}_{n+\frac{1}{2}}, \boldsymbol{C}_{i,n+\frac{1}{2}}\Big),$$

and the external data are evaluated at the midpoint, $\boldsymbol{b}_{0,n+\frac{1}{2}} := \boldsymbol{b}_0(\cdot, t_{n+\frac{1}{2}})$ and $\bar{\boldsymbol{t}}_{0,n+\frac{1}{2}} := \bar{\boldsymbol{t}}_0(\cdot, t_{n+\frac{1}{2}})$. Choosing $\delta\boldsymbol{\varphi}$ piecewise constant on $[t_n, t_{n+1}]$, the weak form (38) leads to the time-discrete counterpart

$$\int_{\mathcal{B}_0} \rho_0\, \delta\boldsymbol{\varphi} \cdot \boldsymbol{a}_{n+\frac{1}{2}}\, \mathrm{d}V + \int_{\mathcal{B}_0} \boldsymbol{P}_{n+\frac{1}{2}} : \nabla_X(\delta\boldsymbol{\varphi})\, \mathrm{d}V = \int_{\mathcal{B}_0} \rho_0\, \boldsymbol{b}_{0,n+\frac{1}{2}} \cdot \delta\boldsymbol{\varphi}\, \mathrm{d}V + \int_{\partial\mathcal{B}_0^{\mathrm{N}}} \bar{\boldsymbol{t}}_{0,n+\frac{1}{2}} \cdot \delta\boldsymbol{\varphi}\, \mathrm{d}A. \tag{40}$$

Equation (40) is the midpoint-discrete weak form of the momentum balance and will later give rise, after spatial discretization, to the global equilibrium residual $\boldsymbol{R}_q(\boldsymbol{q}^{n+1}, \boldsymbol{C}_i^{n+1})$ in the monolithic Newton system.

The corresponding midpoint thermodynamic driving force is obtained from the free energy as

$$\boldsymbol{M}_{n+\frac{1}{2}} := \boldsymbol{M}\Big(\boldsymbol{C}_{n+\frac{1}{2}}, \boldsymbol{C}_{i,n+\frac{1}{2}}\Big) = 2\, \frac{\partial \Psi_{\mathrm{neq}}}{\partial \boldsymbol{C}_e}\Big(\boldsymbol{C}_{e,n+\frac{1}{2}}\Big)\, \boldsymbol{C}_{i,n+\frac{1}{2}}^{-1}\, \boldsymbol{C}_{n+\frac{1}{2}}. \tag{41}$$

Moreover, we approximate the rate of the internal variable by the difference quotient,

$$\dot{\boldsymbol{C}}_i(\cdot, t_{n+\frac{1}{2}}) \approx \frac{\boldsymbol{C}_i^{n+1} - \boldsymbol{C}_i^{n}}{h},$$

Restricting the weak evolution equation (39) to the interval $[t_n, t_{n+1}]$ gives

$$\int_{\mathcal{B}_0} \delta\boldsymbol{\Sigma} : \Big(\frac{\boldsymbol{C}_i^{n+1} - \boldsymbol{C}_i^{n}}{h} - 2\, \boldsymbol{C}_{i,n+\frac{1}{2}}\, \mathbb{V}^{-1} : \boldsymbol{M}_{n+\frac{1}{2}}^{T}\Big)\, \mathrm{d}V = 0 \quad \forall\, \delta\boldsymbol{\Sigma}, \tag{42}$$

where $\delta\boldsymbol{\Sigma}$ is also piecewise constant on $[t_n, t_{n+1}]$.

3.3 Spatial finite element discretization

So far, the weak forms (40) and (42) are continuous in space. We now introduce a standard finite element approximation on the reference configuration $\mathcal{B}_0$. Let $\mathcal{B}_0$ be decomposed into finite elements $\mathcal{B}_0^e$ with nodal points $a \in \mathcal{I}^e$, and let $N_a(\boldsymbol{X})$ denote the usual C^0 Lagrange shape functions associated with the displacement field. The discrete motion at time t_n is approximated by

$$\delta\boldsymbol{\varphi}_h(\boldsymbol{X}) = \sum_{a \in \mathcal{I}} N_a(\boldsymbol{X})\, \delta\boldsymbol{q}_a, \qquad \boldsymbol{\varphi}_h^n(\boldsymbol{X}) = \sum_{b \in \mathcal{I}} N_b(\boldsymbol{X})\, \boldsymbol{q}_b^n,$$

where $\boldsymbol{q}_b^n$ are the nodal positions (or displacements) and $\delta\boldsymbol{q}_a$ are the corresponding virtual nodal variations. The midpoint kinematics follow from the same interpolation,

$$\boldsymbol{\varphi}_{h,n+\frac{1}{2}} := \tfrac{1}{2}(\boldsymbol{\varphi}_h^{n+1} + \boldsymbol{\varphi}_h^n), \qquad \boldsymbol{F}_{h,n+\frac{1}{2}} := \nabla_X(\boldsymbol{\varphi}_{h,n+\frac{1}{2}}), \qquad \boldsymbol{C}_h^{n+\frac{1}{2}} := \boldsymbol{F}_{h,n+\frac{1}{2}}^{\mathsf{T}}\boldsymbol{F}_{h,n+\frac{1}{2}}.$$

For the internal variable and its thermodynamic driving force we introduce, in general, an approximation space with shape functions $H_\alpha(\boldsymbol{X})$:

$$\delta\boldsymbol{\Sigma}_h(\boldsymbol{X}) = \sum_{\alpha\in\mathcal{J}} H_\alpha(\boldsymbol{X})\,\delta\boldsymbol{\Sigma}_\alpha,$$

and

$$\boldsymbol{C}_{i,h}^{n+\frac{1}{2}}(\boldsymbol{X}) = \sum_{\beta\in\mathcal{J}} H_\beta(\boldsymbol{X})\,\boldsymbol{C}_{i,\beta}^{n+\frac{1}{2}}.$$

The same basis H_β is used for $\boldsymbol{C}_{i,h}^{n+\frac{1}{2}}$ and $\delta\boldsymbol{\Sigma}_h$ for notational convenience; in particular, it may be chosen elementwise discontinuous as we do not require C^0 continuity. The full discrete elastic measure reads

$$\boldsymbol{C}_{e,h}^{n+\frac{1}{2}} := \boldsymbol{C}_h^{n+\frac{1}{2}}\,\boldsymbol{C}_{i,h}^{-1,n+\frac{1}{2}},$$

and the discrete thermodynamic driving force $\boldsymbol{M}_h^{n+\frac{1}{2}} = \boldsymbol{M}\big(\boldsymbol{C}_h^{n+\frac{1}{2}}, \boldsymbol{C}_{i,h}^{n+\frac{1}{2}}\big)$ follows from the free energy as presented in Section 2.2.

Full-discrete momentum equation. Inserting $\boldsymbol{\varphi}_h$, $\delta\boldsymbol{\varphi}_h$ and the midpoint quantities into (40) and exploiting the arbitrariness of the nodal variations $\delta\boldsymbol{q}_a$ yields the full-discrete balance of momentum

$$\sum_{a\in\mathcal{N}} \delta\boldsymbol{q}_a \cdot \boldsymbol{R}_{q,a}^{n+1} = 0 \quad \forall\,\{\delta\boldsymbol{q}_a\}, \tag{43}$$

with nodal residuals

$$\begin{aligned}\boldsymbol{R}_{q,a}^{n+1} := &\int_{\mathcal{B}_0} \rho_0\, N_a\, \boldsymbol{a}_{n+\frac{1}{2}}\,\mathrm{d}V + \int_{\mathcal{B}_0} \boldsymbol{P}_h^{n+\frac{1}{2}} : \nabla_X(N_a)\,\mathrm{d}V \\ &- \int_{\mathcal{B}_0} \rho_0\, N_a\, \boldsymbol{b}_{0,n+\frac{1}{2}}\,\mathrm{d}V - \int_{\partial\mathcal{B}_0^{\mathrm{N}}} N_a\, \bar{\boldsymbol{t}}_{0,n+\frac{1}{2}}\,\mathrm{d}A,\end{aligned} \tag{44}$$

where $\boldsymbol{P}_h^{n+\frac{1}{2}} := \boldsymbol{F}_{h,n+\frac{1}{2}}\boldsymbol{S}(\boldsymbol{C}_h^{n+\frac{1}{2}}, \boldsymbol{C}_{i,h}^{n+\frac{1}{2}})$.

Collecting the nodal residuals in a global vector $\boldsymbol{R}_q^{n+1}$ and the nodal unknowns in $\boldsymbol{q}^{n+1}$ for every node $a \in \mathcal{I}$ and $\mathcal{C}_i^{n+1} := \mathrm{vec}(\boldsymbol{C}_i^{n+1}) \in \mathbb{R}^6$ for every node $\alpha \in \mathcal{J}$, leads to the usual nonlinear algebraic system $\boldsymbol{R}_q^{n+1}(\boldsymbol{q}^{n+1}, \mathcal{C}_i^{n+1}) = \boldsymbol{0}$.

Full-discrete evolution equation. Analogously, inserting the finite element approximations $\boldsymbol{C}_{i,h}$ and $\delta\boldsymbol{\Sigma}_h$ into the midpoint weak evolution equation (42) and using the arbitrariness of the coefficients $\delta\boldsymbol{\Sigma}_\alpha$ yields

$$\sum_{\alpha\in\mathcal{J}} \delta\boldsymbol{\Sigma}_\alpha : \boldsymbol{R}_{\mathrm{visc},\alpha}^{n+1} = 0, \tag{45}$$

with viscous residuals

$$\boldsymbol{R}_{\mathrm{visc},\alpha}^{n+1} := \int_{\mathcal{B}_0} H_\alpha(\boldsymbol{X}) \Big(\frac{\boldsymbol{C}_{i,h}^{n+1} - \boldsymbol{C}_{i,h}^{n}}{h} - 2\,\boldsymbol{C}_{i,h}^{n+\frac{1}{2}}\,\mathbb{V}^{-1} : \boldsymbol{M}_h^{n+\frac{1}{2},T} \Big)\,\mathrm{d}V. \tag{46}$$

Collecting all $\boldsymbol{R}_{\mathrm{visc},\alpha}^{n+1}$ in a global vector $\boldsymbol{R}_{\mathrm{visc}}^{n+1} = \bigcup_\alpha \mathrm{vec}\left(\boldsymbol{R}_{\mathrm{visc},\alpha}^{n+1}\right)$ leads to the full-discrete evolution equation $\boldsymbol{R}_{\mathrm{visc}}^{n+1}(\boldsymbol{q}^{n+1}, \mathcal{C}_i^{n+1}) = \boldsymbol{0}$. At this stage, the choice of the internal-variable shape functions H_β is still completely general. In the classical quadrature point based setting, one chooses H_β discontinuous approximation of the internal variable in the sense of Dirac-type test functions for $\delta\boldsymbol{\Sigma}_h$. Moreover, Kronecker delta functions, the discrete analogs of the Dirac-type pulses, are applied on $\boldsymbol{C}_{i,h}^{n+1}$, such that the viscous residuals reduce to purely local algebraic equations

$$\frac{\boldsymbol{C}_{i,h}^{n+1} - \boldsymbol{C}_{i,h}^{n}}{h} - 2\boldsymbol{C}_{i,h}^{n+\frac{1}{2}}\,\mathbb{V}^{-1} : \boldsymbol{M}_h^{n+\frac{1}{2},T} = \boldsymbol{0},$$

at each quadrature point. This specialization will be discussed later in the context of the monolithic Newton system and the condensation of the internal variables.

3.4 Role of the evolution law in the coupled problem

Equations (44) and (46) define the weak form of the coupled viscoelastic problem on the time interval $[t_n, t_{n+1}]$. From the continuum viewpoint, (39) is a constitutive ODE for $\boldsymbol{C}_i$ enforced by thermodynamics. From the perspective of the fully discrete nonlinear system, however, the relation (46) appears as an additional set of algebraic equations at time t_{n+1}.

In other words, the evolution law acts as an internal constraint in the space of discrete configurations $(\boldsymbol{q}^{n+1}, \mathcal{C}_i^{n+1})$. This interpretation is crucial for the monolithic treatment of the coupled problem: it allows us to assemble a single Newton system for both primary variables and, subsequently, to condense the internal variable $\boldsymbol{C}_i$ by Schur complements or null-space projectors without ever performing a staggered update at the level of the material law.

4 Monolithic Newton system and condensation of the internal variable

Based on the midpoint-discrete weak forms of the momentum balance and the evolution equation, we now assemble the fully discrete nonlinear system at time t_{n+1} and discuss its monolithic solution by Newton's method. Therefore, we consider the fully discrete nonlinear problem with primary unknowns

$$\boldsymbol{z}^{n+1} = \begin{bmatrix} \boldsymbol{q}^{n+1} \\ \mathcal{C}_i^{n+1} \end{bmatrix}.$$

The coupled residual is then

$$\boldsymbol{R}(\boldsymbol{z}^{n+1}) = \begin{bmatrix} \boldsymbol{R}_q(\boldsymbol{q}^{n+1}, \mathcal{C}_i^{n+1}) \\ \boldsymbol{R}_{\text{visc}}(\boldsymbol{q}^{n+1}, \mathcal{C}_i^{n+1}) \end{bmatrix},$$

which has to be fulfilled up to the chosen Newton stopping criterion. In the following, we suppress the time index $n+1$ and, for brevity, the subscript i on the internal variable whenever possible. We denote the viscous residual by $\boldsymbol{R}_{\text{visc}} \equiv \boldsymbol{R}_{\mathcal{C}}$ and use the block notation

$$\boldsymbol{K}_{\alpha\beta} := \frac{\partial \boldsymbol{R}_\alpha}{\partial \beta}, \quad \alpha, \beta \in \{q, \mathcal{C}\}$$

where the first index refers to the residual being linearized and the second index to the variable. In particular, $\boldsymbol{K}_{\mathcal{C}\mathcal{C}}$ denotes the linearization of $\boldsymbol{R}_{\mathcal{C}}$ with respect to $\mathcal{C}$.

4.1 Monolithic Newton system

Linearizing the residual yields the block system

$$\begin{bmatrix} \boldsymbol{K}_{qq} & \boldsymbol{K}_{q\mathcal{C}} \\ \boldsymbol{K}_{\mathcal{C}q} & \boldsymbol{K}_{\mathcal{C}\mathcal{C}} \end{bmatrix} \begin{bmatrix} \Delta \boldsymbol{q} \\ \Delta \mathcal{C} \end{bmatrix} = - \begin{bmatrix} \boldsymbol{R}_q \\ \boldsymbol{R}_{\mathcal{C}} \end{bmatrix}. \tag{47}$$

The blocks have the following interpretations:

- $\boldsymbol{K}_{qq}$: stiffness-like tangent from equilibrium equation,
- $\boldsymbol{K}_{q\mathcal{C}}$: sensitivity of internal forces to the internal variable,
- $\boldsymbol{K}_{\mathcal{C}q}$: sensitivity of evolution equation to the deformation,
- $\boldsymbol{K}_{\mathcal{C}\mathcal{C}}$: tangent of the evolution equation.

In general,

$$\boldsymbol{K}_{q\mathcal{C}} \neq \boldsymbol{K}_{\mathcal{C}q}^{\mathrm{T}},$$

since the evolution law for $\mathcal{C}_i$ is a constitutive ODE rather than a variational constraint; hence the monolithic tangent is non-symmetric.

4.2 Condensation via the Schur complement

The block system (47) can be solved for $\Delta\mathcal{C}$. In particular, from the second row we obtain

$$\Delta\mathcal{C} = -\boldsymbol{K}_{\mathcal{C}\mathcal{C}}^{-1}\boldsymbol{R}_{\mathcal{C}} - \boldsymbol{K}_{\mathcal{C}\mathcal{C}}^{-1}\boldsymbol{K}_{\mathcal{C}q}\,\Delta\boldsymbol{q}. \tag{48}$$

Obviously, one should favor a block-diagonal structure of $\boldsymbol{K}_{\mathcal{C}\mathcal{C}}$. This is naturally obtained in the classical quadrature based discretization, where the internal variables are stored locally and the corresponding shape functions are of Dirac type. Other (discontinuous) choices are possible, e.g. piecewise constant or piecewise linear shape functions.

Insertion into the first row yields

$$\boldsymbol{K}_{qq}\,\Delta\boldsymbol{q} + \boldsymbol{K}_{q\mathcal{C}}\Big(-\boldsymbol{K}_{\mathcal{C}\mathcal{C}}^{-1}\boldsymbol{R}_{\mathcal{C}} - \boldsymbol{K}_{\mathcal{C}\mathcal{C}}^{-1}\boldsymbol{K}_{\mathcal{C}q}\,\Delta\boldsymbol{q}\Big) = -\boldsymbol{R}_q. \tag{49}$$

Collecting the terms in $\Delta\boldsymbol{q}$ yields the condensed system

$$\underbrace{\Big(\boldsymbol{K}_{qq} - \boldsymbol{K}_{q\mathcal{C}}\boldsymbol{K}_{\mathcal{C}\mathcal{C}}^{-1}\boldsymbol{K}_{\mathcal{C}q}\Big)}_{\boldsymbol{K}_{qq}^{\mathrm{cond}}}\Delta\boldsymbol{q} = -\Big(\boldsymbol{R}_q - \boldsymbol{K}_{q\mathcal{C}}\boldsymbol{K}_{\mathcal{C}\mathcal{C}}^{-1}\boldsymbol{R}_{\mathcal{C}}\Big). \tag{50}$$

The matrix $\boldsymbol{K}_{qq}^{\mathrm{cond}}$ is the Schur complement of the internal variable block. Once $\Delta\boldsymbol{q}$ is computed, $\Delta\mathcal{C}$ is recovered from (48). Therefore, storage of the factorization of $\boldsymbol{K}_{\mathcal{C}\mathcal{C}}$ should be considered.

Classical (nested) Gauss-point condensation. In the classical quadrature-point setting, the internal variable is eliminated by enforcing the internal equation locally (and nonlinearly) at every integration point. More precisely, for a given iterate $\boldsymbol{q}^{(k)}$ one solves

$$\boldsymbol{R}_{\mathcal{C}}\Big(\boldsymbol{q}^{(k)}, \mathcal{C}\Big) = \boldsymbol{0} \tag{51}$$

by a local Newton method at each Gauss point up to an internal tolerance ϵ_{int}. This yields an (implicit) solution $\mathcal{C}^\star(\boldsymbol{q})$ and hence a reduced equilibrium residual $\widehat{\boldsymbol{R}}_q(\boldsymbol{q}) := \boldsymbol{R}_q(\boldsymbol{q}, \mathcal{C}^\star(\boldsymbol{q}))$. This leads to the condensed tangent

$$\widehat{\boldsymbol{K}}_{qq} = \frac{\partial \widehat{\boldsymbol{R}}_q}{\partial \boldsymbol{q}} = \boldsymbol{K}_{qq} - \boldsymbol{K}_{q\mathcal{C}}\,\boldsymbol{K}_{\mathcal{C}\mathcal{C}}^{-1}\,\boldsymbol{K}_{\mathcal{C}q}, \tag{52}$$

which coincides with the Schur complement $\boldsymbol{K}_{qq}^{\mathrm{cond}}$ in (50). However, because the classical scheme enforces $\boldsymbol{R}_{\mathcal{C}} = \boldsymbol{0}$ before assembling the global step, the right-hand side reduces to $-\boldsymbol{R}_q$ and (50) becomes

$$\boldsymbol{K}_{qq}^{\mathrm{cond}}\,\Delta\boldsymbol{q} = -\boldsymbol{R}_q. \tag{53}$$

In contrast, the monolithic condensation retains the coupling term $-\boldsymbol{K}_{q\mathcal{C}}\boldsymbol{K}_{\mathcal{C}\mathcal{C}}^{-1}\boldsymbol{R}_{\mathcal{C}}$, which accounts for non-vanishing internal residuals during the global Newton iterations and avoids a nested local Newton solve at each quadrature point.

4.3 Condensation via a null-space operator

The Schur complement (50) can also be written in operator form, which provides a geometric interpretation in terms of the tangent space of the internal constraint.

Row operator and Schur form. We first introduce a row condensation operator that eliminates the internal variable from the linear system. Define

$$\boldsymbol{P}_{\text{row}} := \begin{bmatrix} \boldsymbol{I} & -\boldsymbol{K}_{q\mathcal{C}}\,\boldsymbol{K}_{\mathcal{C}\mathcal{C}}^{-1} \end{bmatrix}.$$

A short block computation shows that

$$\boldsymbol{P}_{\text{row}}\,\boldsymbol{K} = \begin{bmatrix} \boldsymbol{K}_{qq} - \boldsymbol{K}_{q\mathcal{C}}\boldsymbol{K}_{\mathcal{C}\mathcal{C}}^{-1}\boldsymbol{K}_{\mathcal{C}q} & \boldsymbol{0} \end{bmatrix}.$$

Multiplying (47) from the left with $\boldsymbol{P}_{\text{row}}$ gives

$$\boldsymbol{P}_{\text{row}}\,\boldsymbol{K}\,\Delta\boldsymbol{z} = -\boldsymbol{P}_{\text{row}}\,\boldsymbol{R}, \qquad \boldsymbol{R} = \begin{bmatrix} \boldsymbol{R}_q \\ \boldsymbol{R}_{\mathcal{C}} \end{bmatrix},$$

such that we obtain

$$\Big(\boldsymbol{K}_{qq} - \boldsymbol{K}_{q\mathcal{C}}\boldsymbol{K}_{\mathcal{C}\mathcal{C}}^{-1}\boldsymbol{K}_{\mathcal{C}q}\Big)\Delta\boldsymbol{q} = -\Big(\boldsymbol{R}_q - \boldsymbol{K}_{q\mathcal{C}}\boldsymbol{K}_{\mathcal{C}\mathcal{C}}^{-1}\boldsymbol{R}_{\mathcal{C}}\Big),$$

which is exactly the condensed system (50).

Null-space basis and tangent space. Next, we regard the linearized evolution equation as a constraint for the admissible Newton increments. The second block row of (47) reads

$$\boldsymbol{R}_{\mathcal{C}} + \boldsymbol{K}_{\mathcal{C}q}\,\Delta\boldsymbol{q} + \boldsymbol{K}_{\mathcal{C}\mathcal{C}}\,\Delta\mathcal{C} = \boldsymbol{0},$$

and can be written in abstract form as

$$\boldsymbol{R}_{\mathcal{C}} + \boldsymbol{L}\,\Delta\boldsymbol{z} = \boldsymbol{0}, \quad \text{where} \quad \boldsymbol{L} := \begin{bmatrix} \boldsymbol{K}_{\mathcal{C}q} & \boldsymbol{K}_{\mathcal{C}\mathcal{C}} \end{bmatrix}.$$

At a converged solution we have $\boldsymbol{R}_{\mathcal{C}} = \boldsymbol{0}$, and the tangent space of the constraint manifold is characterized by the homogeneous equation $\boldsymbol{L}\,\Delta\boldsymbol{z} = \boldsymbol{0}$. A basis of admissible increments is provided by the column operator

$$\boldsymbol{P}_{\text{col}} := \begin{bmatrix} \boldsymbol{I} \\ -\boldsymbol{K}_{\mathcal{C}\mathcal{C}}^{-1}\,\boldsymbol{K}_{\mathcal{C}q} \end{bmatrix}, \qquad \Delta\boldsymbol{z} = \boldsymbol{P}_{\text{col}}\,\Delta\boldsymbol{q},$$

since

$$\boldsymbol{L}\,\boldsymbol{P}_{\text{col}} = \begin{bmatrix} \boldsymbol{K}_{\mathcal{C}q} & \boldsymbol{K}_{\mathcal{C}\mathcal{C}} \end{bmatrix} \begin{bmatrix} \boldsymbol{I} \\ -\boldsymbol{K}_{\mathcal{C}\mathcal{C}}^{-1}\,\boldsymbol{K}_{\mathcal{C}q} \end{bmatrix} = \boldsymbol{K}_{\mathcal{C}q} - \boldsymbol{K}_{\mathcal{C}\mathcal{C}}\boldsymbol{K}_{\mathcal{C}\mathcal{C}}^{-1}\boldsymbol{K}_{\mathcal{C}q} = \boldsymbol{0}.$$

Restricting the Newton increment to this tangent space and testing the linear system with the row operator yields the reduced system

$$\boldsymbol{P}_{\text{row}}\,\boldsymbol{K}\,\boldsymbol{P}_{\text{col}}\,\Delta\boldsymbol{q} = -\,\boldsymbol{P}_{\text{row}}\,\boldsymbol{R}. \tag{54}$$

Using the block structure of $\boldsymbol{K}$ and $\boldsymbol{R}$, one readily verifies

$$\boldsymbol{P}_{\text{row}}\,\boldsymbol{K}\,\boldsymbol{P}_{\text{col}} = \boldsymbol{K}_{qq} - \boldsymbol{K}_{q\mathcal{C}}\,\boldsymbol{K}_{\mathcal{C}\mathcal{C}}^{-1}\,\boldsymbol{K}_{\mathcal{C}q}, \qquad \boldsymbol{P}_{\text{row}}\,\boldsymbol{R} = \boldsymbol{R}_q - \boldsymbol{K}_{q\mathcal{C}}\,\boldsymbol{K}_{\mathcal{C}\mathcal{C}}^{-1}\,\boldsymbol{R}_{\mathcal{C}},$$

so that (54) is identical to the Schur complement system (50). Since the monolithic tangent is generally non-symmetric, the left and right operator differ: $\boldsymbol{P}_{\text{col}}$ parameterizes admissible increments in the tangent space of the internal constraint, while $\boldsymbol{P}_{\text{row}}$ selects those test directions in which the internal variables have already been condensed.

Geometric interpretation of the null-space basis. The set of all configurations that satisfy the internal equation defines the internal constraint manifold

$$\mathfrak{M} := \Big\{ \boldsymbol{z} \in \mathbb{R}^{n_q+n_\mathcal{C}} \;\Big|\; \boldsymbol{R}_\mathcal{C}(\boldsymbol{z}) = \boldsymbol{0} \Big\}.$$

Consider a configuration $\boldsymbol{z}^* = (\boldsymbol{q}^*, \mathcal{C}^*)$ on $\mathfrak{M}$, i.e. $\boldsymbol{R}_\mathcal{C}(\boldsymbol{z}^*) = \boldsymbol{0}$. A perturbation $\Delta\boldsymbol{z}$ is admissible in first order if it keeps the constraint satisfied up to quadratic terms,

$$\boldsymbol{R}_\mathcal{C}(\boldsymbol{z}^* + \Delta\boldsymbol{z}) = \mathcal{O}(\|\Delta\boldsymbol{z}\|^2).$$

Linearizing $\boldsymbol{R}_\mathcal{C}$ at $\boldsymbol{z}^*$ yields

$$\boldsymbol{R}_\mathcal{C}(\boldsymbol{z}^* + \Delta\boldsymbol{z}) \approx \boldsymbol{R}_\mathcal{C}(\boldsymbol{z}^*) + \underbrace{\frac{\partial \boldsymbol{R}_\mathcal{C}}{\partial \boldsymbol{z}}(\boldsymbol{z}^*)}_{=[\,\boldsymbol{K}_{\mathcal{C}q} \quad \boldsymbol{K}_{\mathcal{C}\mathcal{C}}\,]} \Delta\boldsymbol{z}.$$

Since $\boldsymbol{R}_\mathcal{C}(\boldsymbol{z}^*) = \boldsymbol{0}$, admissible increments must satisfy the linearized constraint

$$\boldsymbol{K}_{\mathcal{C}q}\,\Delta\boldsymbol{q} + \boldsymbol{K}_{\mathcal{C}\mathcal{C}}\,\Delta\boldsymbol{\mathcal{C}} = \boldsymbol{0}. \tag{55}$$

The tangent space of $\mathfrak{M}$ at $\boldsymbol{z}^*$ is therefore the null-space of the block row $[\,\boldsymbol{K}_{\mathcal{C}q} \;\; \boldsymbol{K}_{\mathcal{C}\mathcal{C}}\,]$,

$$T_{\boldsymbol{z}^*}\mathfrak{M} = \Big\{ \Delta\boldsymbol{z} \;\Big|\; \boldsymbol{K}_{\mathcal{C}q}\,\Delta\boldsymbol{q} + \boldsymbol{K}_{\mathcal{C}\mathcal{C}}\,\Delta\mathcal{C} = \boldsymbol{0} \Big\}.$$

Assuming that $\boldsymbol{K}_{\mathcal{C}\mathcal{C}}$ is nonsingular in the considered regime - which is the same local regularity condition required by the classical local constitutive update - the linearized constraint can be solved for $\Delta\mathcal{C}$ in terms of $\Delta\boldsymbol{q}$ as

$$\Delta\mathcal{C} = -\,\boldsymbol{K}_{\mathcal{C}\mathcal{C}}^{-1}\,\boldsymbol{K}_{\mathcal{C}q}\,\Delta\boldsymbol{q},$$

as shown above. The columns of the matrix $\boldsymbol{P}_{\text{col}}$ therefore form a basis of the null-space of the linearized constraint, and we have the geometric identity

$$\operatorname{Im}(\boldsymbol{P}_{\text{col}}) = \ker \begin{bmatrix} \boldsymbol{K}_{\mathcal{C}q} & \boldsymbol{K}_{\mathcal{C}\mathcal{C}} \end{bmatrix} = T_{\boldsymbol{z}^*}\mathfrak{M}.$$

In this sense, $\boldsymbol{P}_{\text{col}}$ is a null-space basis that spans the tangent space of the internal constraint manifold. The actual reduction of the Newton system is then performed by restricting the increments to this tangent space via $\Delta\boldsymbol{z} = \boldsymbol{P}_{\text{col}}\,\Delta\boldsymbol{q}$ and premultiplying the monolithic system with the row operator $\boldsymbol{P}_{\text{row}}$. The null-space formulation provides a clean geometric interpretation of the Schur complement condensation: Newton steps are confined to the tangent space of the internal constraint manifold, and the condensed operator $\boldsymbol{K}_{qq}^{\text{cond}}$ is precisely the restriction of $\boldsymbol{K}$ to this space.

5 Numerical examples

In this section, we compare the proposed monolithic Newton strategy, in which the internal variable is condensed at the level of the global linearized system, with a classical nested Gauss-point condensation scheme, where the internal evolution equation is solved locally at each quadrature point by an inner Newton loop (see Section 4). Unless stated otherwise, both approaches employ identical spatial discretizations and linear solver settings; any observed differences therefore reflect the nonlinear solution strategy.

Throughout the examples, we employ the finite viscoelastic Simo–Taylor material introduced in Section 2.2. The equilibrium/non-equilibrium split of the free energy density reads

$$\Psi(\boldsymbol{C}, \mathcal{C}_i) = \Psi_{\mathrm{eq}}(\boldsymbol{C}) + \Psi_{\mathrm{neq}}(\boldsymbol{C}_e), \qquad \boldsymbol{C}_e = \boldsymbol{C}\,\mathcal{C}_i^{-1}.$$

In our implementation, the equilibrium part is chosen as

$$\Psi_{\mathrm{eq}}(\boldsymbol{C}) = \frac{\mu}{2}\Big(\mathrm{tr}(\boldsymbol{C}) - d - 2\log(J)\Big) + \frac{\lambda}{2}\Big((\log(J))^2 + (J-1)^2\Big), \qquad J = \sqrt{\det(\boldsymbol{C})},$$

and the non-equilibrium part is of the same form, evaluated at $\boldsymbol{C}_e$,

$$\Psi_{\mathrm{neq}}(\boldsymbol{C}_e) = \frac{\mu_{\mathrm{visc}}}{2}\Big(\mathrm{tr}(\boldsymbol{C}_e) - d - 2\log(J_e)\Big) + \frac{\lambda_{\mathrm{visc}}}{2}\Big((\log(J_e))^2 + (J_e-1)^2\Big), \qquad J_e = \sqrt{\det(\boldsymbol{C}_e)}.$$

Here, d denotes the dimension of the tensor representation used in the constitutive evaluation (in the present examples, $d = 3$ for both plane strain and 3D). The viscous flow is governed by the isotropic viscosity tensor

$$\mathbb{V} = V_{\mathrm{vol}}\,\mathbb{P}_{\mathrm{vol}} + 2V_{\mathrm{dev}}\,\mathbb{P}_{\mathrm{dev}},$$

with parameters listed in Table 1 in terms of area, i.e. scaled by the (unit) thickness.

Density	ρ_0	10 [kg/m^2]
First Lamé constant	λ	30000 [J/m^2]
Second Lamé constant	μ	7500 [J/m^2]
Deviatoric viscosity	V_{dev}	10000 [Js/m^2]
Volumetric viscosity	V_{vol}	50000 [Js/m^2]
Viscous First Lamé constant	λ_{visc}	30000 [J/m^2]
Viscous Second Lamé constant	μ_{visc}	7500 [J/m^2]

Table 1: Material parameters. Note that we have calibrated the set of parameters per area.

5.1 2D Cook's membrane

We consider the two-dimensional Cook's membrane benchmark on the reference domain defined by the corner points $\boldsymbol{P}_1 = (0, 0)$, $\boldsymbol{P}_2 = (480, 440)$, $\boldsymbol{P}_3 = (480, 600)$, and $\boldsymbol{P}_4 =$

$(0, 440)$, given in [mm] with an initial velocity of zero. A plane-strain setting is adopted by embedding the in-plane deformation gradient into three dimensions,

$$\boldsymbol{F} = \begin{bmatrix} \boldsymbol{F}_{2D} & \boldsymbol{0} \\ \boldsymbol{0} & 1 \end{bmatrix}.$$

With this choice, the standard three-dimensional kinematic relations reduce consistently to plane strain; in particular, the out-of-plane stretch remains fixed and the determinant is fully determined by the in-plane part. Details of the corresponding plane-strain reduction, including the cofactor structure, can be found in [9].

Homogeneous Dirichlet boundary conditions are prescribed on the left edge,

$$\Gamma^{\varphi} := \{\, \boldsymbol{X} \in \mathbb{R}^2 \mid X_1 = 0,\ 0 < X_2 < 440 \,\},$$

which is fixed. On the right edge,

$$\Gamma^{\sigma}_r := \{\, \boldsymbol{X} \in \mathbb{R}^2 \mid X_1 = 480,\ 440 < X_2 < 600 \,\},$$

we prescribe the time-dependent surface traction

$$\bar{\boldsymbol{T}} := (-750,\, 1000), \qquad \Lambda(t) = \begin{cases} t/T_{\text{end}}, & 0 \le t \le T_{\text{end}}, \\ 1, & t > T_{\text{end}}, \end{cases}$$

such that

$$\boldsymbol{T}(\boldsymbol{X}, t) = \Lambda(t)\, p\, \bar{\boldsymbol{T}} \qquad \forall\, \boldsymbol{X} \in \Gamma^{\sigma}_r.$$

Body forces are set to $\boldsymbol{B} = \boldsymbol{0}$.

The deformation is interpolated with bilinear Lagrange shape functions (Q1 elements). The internal variable $\mathcal{C}_i$ is stored locally at quadrature points, cf. Section 3.3. This yields a block-diagonal structure of $\boldsymbol{K}_{\mathcal{C}\mathcal{C}}$ and enables efficient condensation. The mesh consists of 20×20 bilinear Q1 elements with four Gauss points per element.

A time interval of $T_{\text{end}} = 10\,\text{s}$ is considered and discretized by $n = 10$ time steps, resulting in a step size $\Delta t = 1\,\text{s}$. For the classical nested condensation scheme, the tolerance of the local (internal) Newton solve is set to $\epsilon_{\text{int}} = 10^{-12}$, whereas the tolerance of the global (external) Newton solve is set to $\epsilon_{\text{ext}} = 10^{-9}$. For the monolithic strategy, a single global tolerance $\epsilon = 10^{-9}$ is used.

Table 2: Average number of Newton iterations per time step for the 2D Cook's membrane.

	p		
Solution strategy	1	2	4
Monolithic	4.0	4.7	4.9
Classical (nested condensation)	4.0 (13.5)	4.7 (15.9)	4.8 (17.2)

Table 2 reports the average number of outer Newton iterations per time step. For the classical nested condensation scheme, the values in parentheses denote the average number of local Newton iterations per quadrature point and time step.

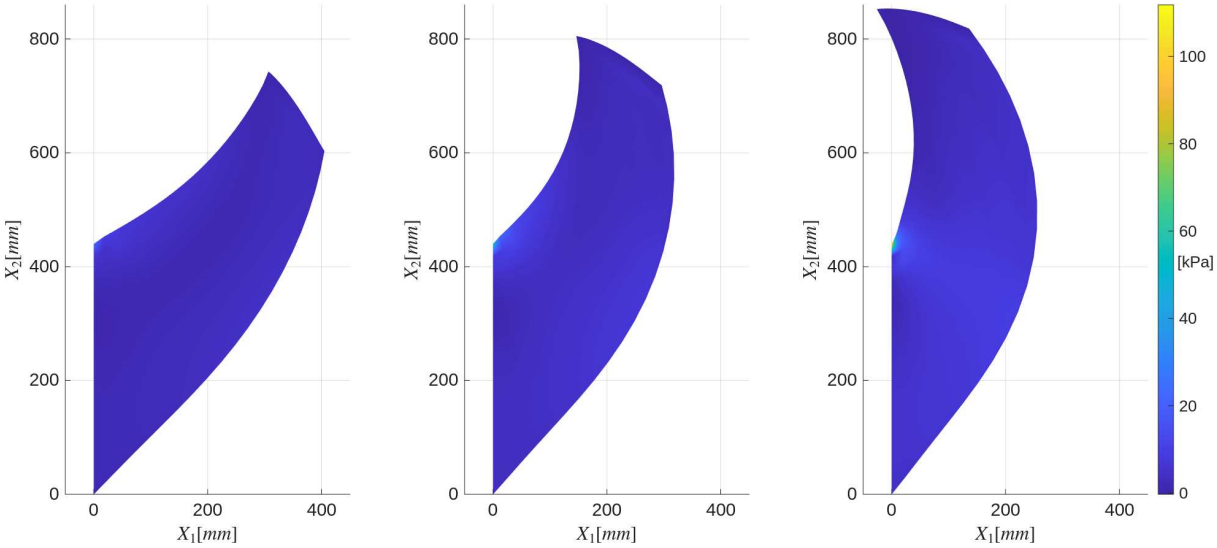


Figure 1. Deformed configurations of Cook's membrane for $p = 1, 2$, and 4. Colors indicate the Frobenius Norm of the First Piola-Kirchhoff stresses in [kPa].

For the three load multipliers $p = 1, 2, 4$, the wall-clock times of the monolithic strategy are 38.53 s, 43.09 s, and 47.06 s, respectively, whereas the classical nested condensation requires 71.71 s, 81.22 s, and 84.84 s. Thus, for this example, the monolithic strategy is approximately twice as fast, mainly because it avoids repeated local Newton solves at all quadrature points. All computations were carried out in Matlab R2025a with a direct solver using two Xeon E5-2640v4 at 2,4GHz and Ubuntu 20.04. Although absolute runtimes are implementation dependent, the additional local iteration work of the nested strategy is intrinsic, so the qualitative performance trend is robust. We further note that the tighter local tolerance $\epsilon_{\text{int}} = 10^{-12}$ does not materially affect this comparison: in the present computations, the local Newton residual typically drops from about $10^{-6} - 10^{-7}$ directly to 10^{-13}–10^{-14} in the final iteration, so that replacing $\epsilon_{\text{int}} = 10^{-12}$ by 10^{-9} changes the overall wall-clock time only negligibly.

As an illustration, Table 3 compares representative Newton convergence histories in the first and last time steps. The monolithic column reports the norm of the global residual. For the classical nested condensation scheme, we list the global (external) residual together with the residual history of the local (internal) Newton solve at a representative quadrature point.

To verify that both approaches yield the same physical response, we additionally perform a relaxation-extension test for $p = 1$. The prescribed surface traction is ramped over $0 \leq t \leq 10$ s and then kept constant over $10 < t \leq 15$ s. Figure 2 shows the total strain energy together with the incremental and cumulative internal dissipation and the kinetic energy over the full loading history. The legend entries I and II refer to the monolithic and classical nested-condensation strategies, respectively. The curves are indistinguishable on the scale of the figure, confirming that both approaches produce the same mechanical response and differ only in the nonlinear solution procedure.

Table 3: Representative Newton convergence histories (time step 1 and 10).

k	Time step 1		
	Monolithic	Classical (nested)	
		External Newton	Internal Newton
0	4.41×10^{0}	4.42×10^{0}	8.57×10^{-16}
1	2.21×10^{1}	1.76×10^{1}	7.95×10^{-3} 5.08×10^{-7} 1.23×10^{-15}
2	6.74×10^{-3}	9.79×10^{-3}	7.98×10^{-3} 5.09×10^{-7} 1.06×10^{-15}
3	9.89×10^{-6}	5.09×10^{-6}	7.99×10^{-3} 5.10×10^{-7} 9.96×10^{-16}
4	5.04×10^{-10}	4.26×10^{-10}	7.99×10^{-3} 5.10×10^{-7} 1.03×10^{-15}

5.2 3D Cook's membrane

We next consider the 3D Cook's membrane benchmark to assess the robustness of the proposed solver in a genuinely three-dimensional setting. The reference configuration is defined by the corner points $\boldsymbol{P}_1 = (0, 0, 0)$, $\boldsymbol{P}_2 = (480, 440, 0)$, $\boldsymbol{P}_3 = (480, 600, 0)$, $\boldsymbol{P}_4 = (0, 440, 0)$, $\boldsymbol{P}_5 = (0, 0, 160)$, $\boldsymbol{P}_6 = (480, 440, 160)$, $\boldsymbol{P}_7 = (480, 600, 160)$, and $\boldsymbol{P}_8 = (0, 440, 160)$.

Again, the left face

$$\Gamma^{\varphi} := \{\, \boldsymbol{X} \in \mathbb{R}^3 \mid X_1 = 0,\ 0 < X_2 < 440,\ 0 < X_3 < 160 \,\}$$

is fixed. On the right face

$$\Gamma^{\sigma}_r := \{\, \boldsymbol{X} \in \mathbb{R}^3 \mid X_1 = 480,\ 440 < X_2 < 600,\ 0 < X_3 < 160 \,\},$$

we prescribe the time-dependent surface traction

$$\bar{\boldsymbol{T}} := (-750,\ 1000,\ 500), \qquad \Lambda(t) = \begin{cases} t/T_{\text{end}}, & 0 \le t \le T_{\text{end}}, \\ 1, & t > T_{\text{end}}, \end{cases}$$

such that

$$\boldsymbol{T}(\boldsymbol{X}, t) = \Lambda(t)\, p\, \bar{\boldsymbol{T}} \qquad \forall\, \boldsymbol{X} \in \Gamma^{\sigma}_r.$$

Body forces are set to $\boldsymbol{B} = \boldsymbol{0}$.

The same viscoelastic Simo–Taylor material and parameters as in the 2D example are used (Table 1), rewritten in terms of volume instead of area. The deformation is interpolated

Table 4: Representative Newton convergence histories (continued).

k	Time step 10		
	Monolithic	Classical (nested)	
		External Newton	Internal Newton
0	3.07×10^{1}	2.95×10^{1}	3.50×10^{-2} 1.54×10^{-6} 2.63×10^{-15}
1	2.58×10^{1}	2.04×10^{1}	4.70×10^{-2} 2.70×10^{-6} 5.45×10^{-15}
2	1.32×10^{-1}	3.79×10^{-2}	4.72×10^{-2} 2.70×10^{-6} 5.15×10^{-15}
3	8.52×10^{-4}	1.52×10^{-4}	4.72×10^{-2} 2.70×10^{-6} 5.36×10^{-15}
4	5.14×10^{-10}	3.70×10^{-10}	4.72×10^{-2} 2.70×10^{-6} 5.23×10^{-15}

Table 5: Average number of Newton iterations per time step for the 3D Cook's membrane.

Solution strategy	p			
	0.5	1.0	1.5	2.0
Monolithic	6.2	7.6	7.1	7.6
Classical (nested condensation)	5.9 (19.6)	7.2 (27.2)	/	/

by trilinear 8-node hexahedral elements. The internal variable $\mathcal{C}_i$ is again stored locally at the quadrature points, which yields a block-diagonal structure of $\boldsymbol{K}_{\mathcal{C}\mathcal{C}}$ and therefore enables efficient condensation. The mesh consists of $20 \times 20 \times 5$ trilinear hex elements with eight Gauss points per element.

For this 3D example, both strategies employ a line search variant of the Newton method for the global system for all examples, classical as well as the monolithic approach. The global tolerances are set to $\epsilon = \epsilon_{\text{ext}} = 10^{-8}$. A time interval of $T_{\text{end}} = 10\,\text{s}$ is considered and discretized by $n = 13$ time steps, corresponding to a step size $\Delta t = 10/13\,\text{s}$.

Table 5 reports the average number of outer Newton iterations per time step for four load multipliers. A slash indicates that the classical nested condensation did not converge; in particular one or more of the internal Newton iteration diverges. As in the 2D example, the values in parentheses denote the average number of local Newton iterations per quadrature point and time step. Already at the standard discretization with $n = 13$, the 3D example

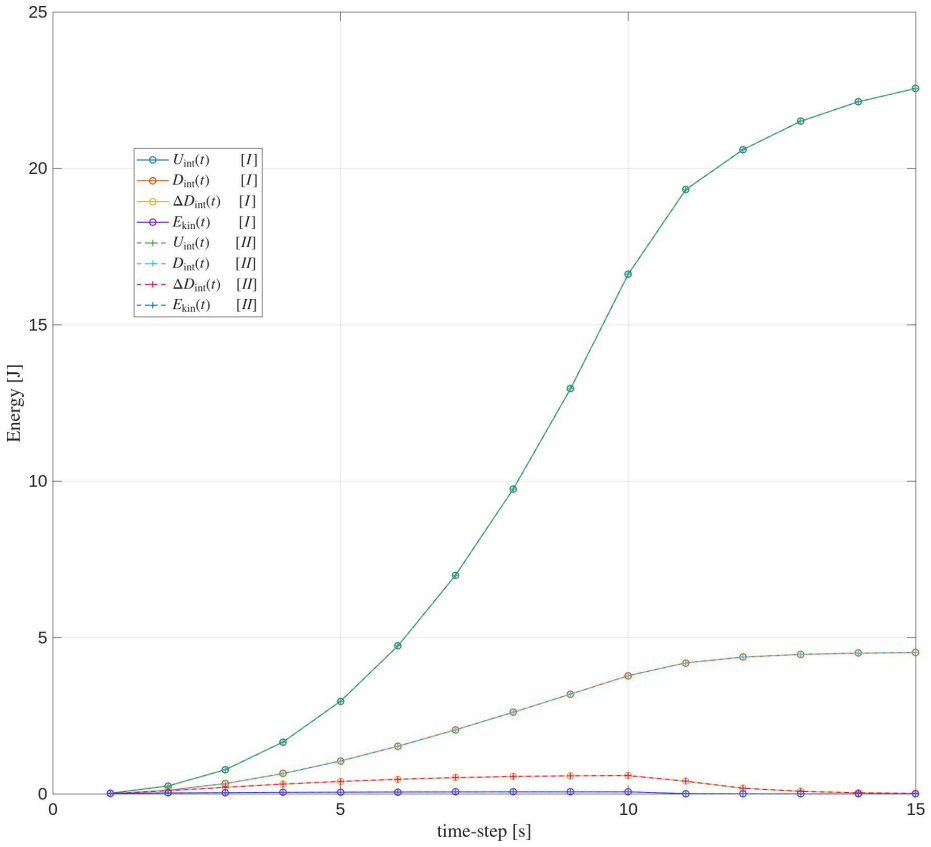


Figure 2. U_{int}, ΔD_{int}, D_{int}, and E_{kin} values for monolithic and classical nested condensation solution strategies versus time step t.

highlights the improved robustness of the monolithic strategy compared to the classical nested Gauss-point scheme.

n \ p	0.5	1.0	1.5	2.0
2	/	/	/	/
3	/	/	/	/
4	10.5	/	/	/
5	9.2	/	/	/
7	7.9	9.1	/	/
8	7.6	8.1	/	/
10	7.1	8.0	8.2	/
11	6.6	7.5	7.5	11.5
12	6.7	7.5	6.9	7.7
13	6.2	7.6	7.1	7.6

Table 6: Newton iteration counts for the Monolithic strategy across different n and p configurations.

To quantify this robustness difference further, the load increment per time step is progressively increased in order to determine the minimum number of time steps, n_{min}, required for convergence. The corresponding results are collected in Tables 6 and 7.

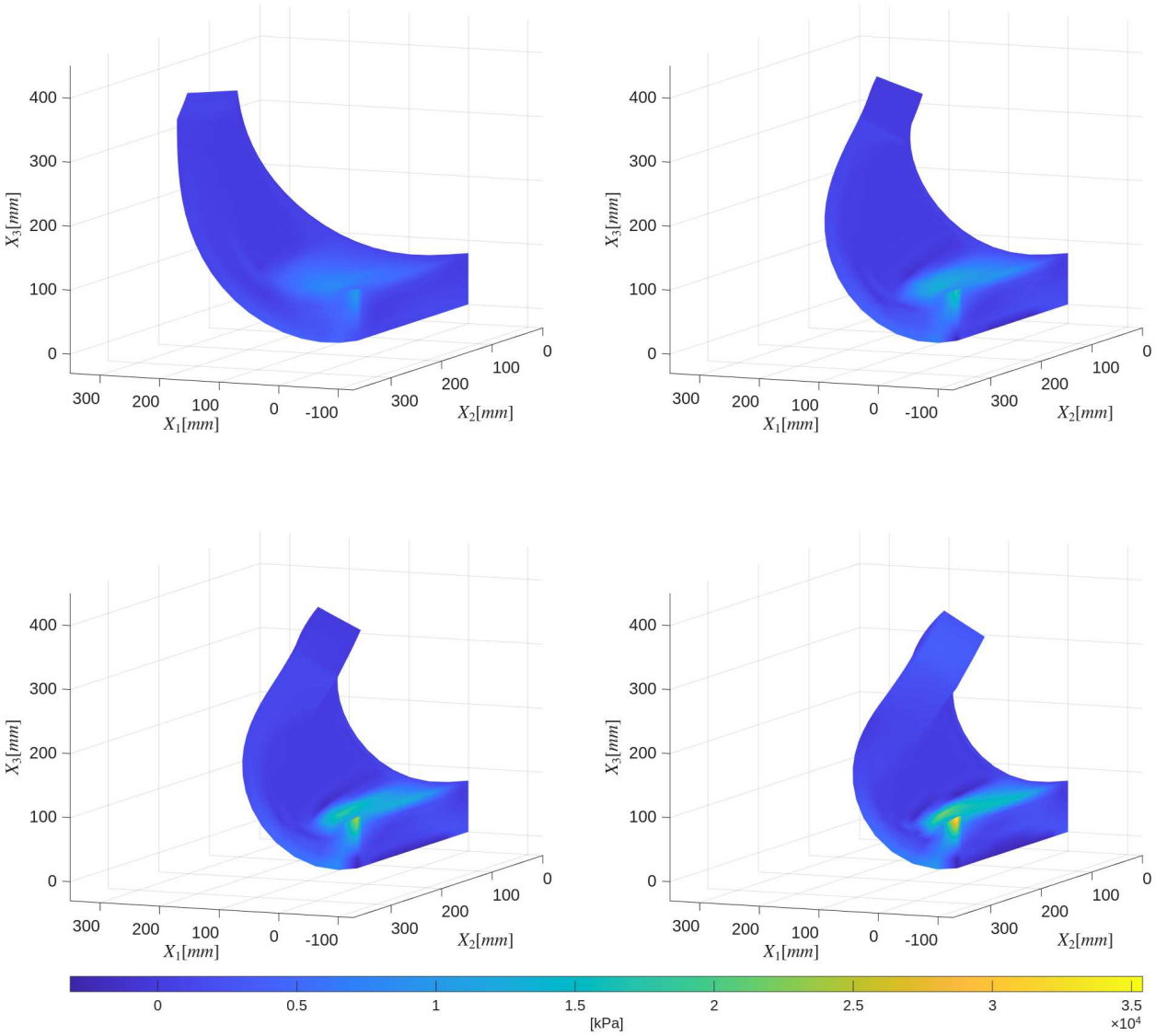


Figure 3. Deformed configurations of the 3D Cook's membrane for $p = 0.5$, 1.0, 1.5, and 2.0. Colors indicate the Frobenius Norm of the First Piola-Kirchhoff stresses in [kPa].

As expected, the average number of Newton iterations increases for both strategies as the load increment per step becomes larger, i.e. as n decreases. For the classical nested approach, the same trend is also visible in the local Newton iterations. More importantly, the difference between both strategies becomes pronounced for larger load multipliers. For $p = 0.5$ and $p = 1.0$, both approaches show comparable robustness, with $n_{\min} = 4$ and $n_{\min} = 7$, respectively. For $p = 1.5$ and $p = 2.0$, however, the monolithic strategy converges already for $n_{\min} = 10$ and $n_{\min} = 11$, whereas the classical nested condensation requires $n_{\min} = 22$ and $n_{\min} = 28$. Hence, for the larger load levels, the nested strategy requires significantly smaller load increments, by factors of 2.2 and 2.54, respectively.

5.3 Discretization study

In this subsection, we investigate how the choice of approximation space for the internal variable $\mathcal{C}_i$ influences the discretization error for the 2D Cook's membrane setup intro-

n \ p	0.5	1.0	1.5	2.0
2	/	/	/	/
3	/	/	/	/
4	9.8 (39.3)	/	/	/
5	9.4 (35.2)	/	/	/
7	8.0 (29.6)	8.9 (33.9)	/	/
10	6.7 (23.0)	7.6 (30.1)	/	/
13	5.9 (19.6)	7.2 (27.3)	/	/
15	5.7 (19.2)	6.7 (23.5)	/	/
20	5.4 (16.9)	6.5 (22.9)	/	/
22	5.2 (16.6)	6.3 (23.5)	6.6 (23.2)	/
25	5.0 (16.1)	5.2 (17.3)	6.2 (20.3)	/
26	4.9 (15.7)	5.2 (16.8)	6.2 (21.7)	/
28	4.8 (15.0)	4.1 (16.6)	6.0 (21.3)	6.1 (21.4)
35	4.5 (14.5)	4.9 (15.6)	4.9 (16.1)	5.5 (18.4)

Table 7: Newton iteration counts for the classical nested condensation strategy across different n and p configurations.

duced in Section 5.1. We compare the six viscoelastic discretization variants

$$m = [m_\varphi, m_{\mathcal{C}_i}] \in \{[1,1], [2,2], [1,c], [2,c], [1,\delta], [2,\delta]\},$$

together with an additional purely elastic reference case, denoted by $[1, x]$, in which the viscous contribution is switched off.

Here, $m_\varphi = 1$ and $m_\varphi = 2$ denote standard C^0 first- and second-order Lagrange interpolations of the displacement field. For the internal variable $\mathcal{C}_i$, no continuity across element boundaries is imposed; the labels $m_{\mathcal{C}_i} = 1$ and $m_{\mathcal{C}_i} = 2$ denote element-wise first- and second-order Lagrange approximations, $m_{\mathcal{C}_i} = c$ denotes an element-wise constant approximation, and $m_{\mathcal{C}_i} = \delta$ denotes the quadrature-point-localized Dirac-pulse approximation introduced in Section 3.3. The additional setting $[1, x]$ serves as a purely elastic reference for the observed convergence behavior.

The boundary conditions and loading are identical to those in the 2D example, with load multiplier $p = 1$. The mesh family consists of the structured grids 10×5, 20×10, 40×20, 80×40, 160×80, and 320×160. For both the viscoelastic discretizations and the purely elastic reference case $[1, x]$, an overkill solution on a 1280×640 mesh is used, i.e. all viscoelastic simulations are compared with a single overkill solution. The nonlinear solver tolerance is set to $\epsilon = 10^{-8}$ for the linear cases and to $\epsilon = 10^{-7}$ for the quadratic and reference computations. We verified that tightening ϵ does not change the curves in Fig. 4.

For each discretization, the error is measured in the displacement field by the L^2-norm

$$e_h := \left(\int_{B_0} \|\varphi_h - \varphi_{\text{ref}}\|^2 \, dV \right)^{1/2},$$

where φ_{ref} denotes the overkill reference solution.

Figure 4 plots the displacement error e_h against the mesh-size parameter h. The additional curve $[1, x]$ provides the purely elastic reference response for the same geometry and loading. The displacement error is dominated by the kinematics discretization; the internal-variable approximation mainly affects cost, not accuracy, for this benchmark.

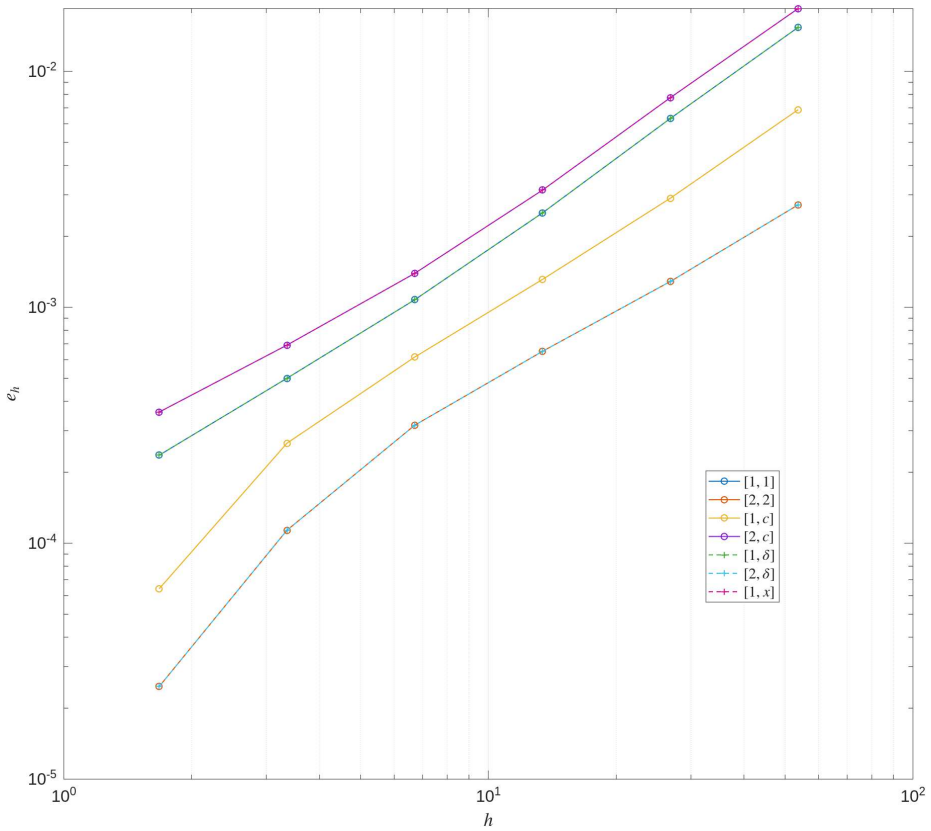


Figure 4. L^2-displacement error versus mesh-size parameter h for the discretization schemes $m = [m_\varphi, m_{\mathcal{C}_i}]$. The additional curve $[1, x]$ denotes the purely elastic reference case with deactivated viscous branch.

The results show that the discretization error is governed primarily by the approximation of the primary field φ. For a fixed interpolation order of φ, changing the approximation space of the internal variable $\mathcal{C}_i$ has only a comparatively small influence on the overall displacement error. In particular, the localized δ-based approximation and the element-wise constant approximation remain very close to the corresponding richer approximations of $\mathcal{C}_i$.

The additional elastic reference curve $[1, x]$ provides a useful baseline for the present geometry and loading and indicates that the observed convergence behavior is already largely determined by the approximation of the displacement field itself. Hence, for the present benchmark, even a very economical approximation of the internal variable is sufficient. In particular, an element-wise constant representation of $\mathcal{C}_i$ already captures the response with essentially the same accuracy trend, while richer approximation spaces for the internal variable do not lead to a commensurate gain in accuracy.

6 Conclusions

We have presented a monolithic solution framework for finite viscoelasticity with a strain-like internal variable and shown that the corresponding internal evolution equations can be condensed systematically at the level of the fully discrete Newton system. Starting from a midpoint time discretization designed to mirror the underlying energy-dissipation structure, the coupled problem in the deformation and the internal variable is written as a single nonlinear system. Its linearization yields a naturally non-symmetric block tangent, which can be used to eliminate the internal-variable increment by a Schur complement. This leads to a reduced system in the displacement unknowns only, while the same reduction admits a clear geometric interpretation through a null-space basis of the tangent space of the internal constraint manifold. In this sense, the proposed formulation provides a genuinely monolithic counterpart to classical local condensation at the material-point level.

The numerical examples show, for the benchmark problems considered, two main advantages of the proposed strategy. For the 2D Cook's membrane, the monolithic treatment requires essentially the same number of outer Newton iterations as the classical nested approach, but avoids repeated local Newton solves at the quadrature points and therefore reduces the overall computational cost substantially. For the 3D Cook's membrane, the monolithic formulation is also more robust: it remains convergent for parameter ranges and load increments for which the nested Gauss-point condensation fails, and it allows significantly larger load steps. The discretization study further indicates that highly localized approximations of the internal variable remain competitive in accuracy while preserving the structural advantages of local condensation, whereas richer approximations may improve accuracy only at the price of a higher nonlinear solution cost.

The present formulation also suggests a natural extension beyond the specific viscoelastic model studied here. Since the fully discrete structure only relies on the availability of a free energy, internal evolution equations, and a consistent material tangent, the same monolithic/condensed strategy should be transferable to broader classes of generalized standard materials, including viscoplastic regularizations of finite-strain plasticity. Future work should focus on a discrete verification of the energy-dissipation balance, on more demanding three-dimensional benchmarks, and on the extension of the present framework to further inelastic constitutive models and tailored linear-solver/preconditioning strategies.

Acknowledgments

Support for this research was provided by the Deutsche Forschungsgemeinschaft (DFG), Germany under grant HE5943/24-1 and HE5943/26-1. This support is gratefully acknowledged.

References

[1] J.S. Bergström and M.C. Boyce. Constitutive modeling of the large strain time-dependent behavior of elastomers. *Journal of the Mechanics and Physics of Solids*, 46(5):931–954, 1998.

[2] J. Bonet. Large strain viscoelastic constitutive models. *International Journal of Solids and Structures*, 38(17):2953–2968, 2001.

[3] Sergio Conde Martin, Juan Carlos Garcia Orden, and Ignacio Romero. Energy-consistent time integration for nonlinear viscoelasticity. *Computational Mechanics*, 54:473–488, 2014.

[4] Fabio De Angelis. An internal variable variational formulation of viscoplasticity. *Computer Methods in Applied Mechanics and Engineering*, 190(1):35–54, 2000.

[5] M. Dittmann, S. Schuß, B. Wohlmuth, and C. Hesch. Weak cn coupling for multi-patch isogeometric analysis in solid mechanics. *International Journal for Numerical Methods in Engineering*, 118(11):678–699, 2019.

[6] M. Gross and P. Betsch. Energy-momentum consistent finite element discretization of dynamic finite viscoelasticity. *International Journal for Numerical Methods in Engineering*, 81:1341–1386, 2010.

[7] Klaus Hackl. Generalized standard media and variational principles in classical and finite strain elastoplasticity. *Journal of the Mechanics and Physics of Solids*, 45(5):667–688, 1997.

[8] Stefan Hartmann. Computation in finite-strain viscoelasticity: finite elements based on the interpretation as differential–algebraic equations. *Computer Methods in Applied Mechanics and Engineering*, 191(13):1439–1470, 2002.

[9] C. Hesch, A.J. Gil, R. Ortigosa, M. Dittmann, C. Bilgen, P. Betsch, M. Franke, A. Janz, and K. Weinberg. A framework for polyconvex large strain phase-field methods to fracture. *Computer Methods in Applied Mechanics and Engineering*, 317:649–683, 2017.

[10] Christian Hesch, Felix Schmidt, and Stefan Schuß. Variational formulation and monolithic solution of computational homogenization methods. *International Journal for Numerical Methods in Engineering*, 125(20):e7567, 2024.

[11] Ustim Khristenko, Stefan Schuß, Melanie Krüger, Felix Schmidt, Barbara Wohlmuth, and Christian Hesch. Multidimensional coupling: A variationally consistent approach to fiber-reinforced materials. *Computer Methods in Applied Mechanics and Engineering*, 382:113869, 2021.

[12] Bernd Kleuter, Andreas Menzel, and Paul Steinmann. Generalized parameter identification for finite viscoelasticity. *Computer Methods in Applied Mechanics and Engineering*, 196(35):3315–3334, 2007.

[13] Patrick Le Tallec, Christophe Rahier, and Ahmed Kaiss. Three-dimensional incompressible viscoelasticity in large strains: Formulation and numerical approximation. *Computer Methods in Applied Mechanics and Engineering*, 109(3):233–258, 1993.

[14] Christian Linder, Mykola Tkachuk, and Christian Miehe. A micromechanically motivated diffusion-based transient network model and its incorporation into finite rubber viscoelasticity. *Journal of the Mechanics and Physics of Solids*, 59(10):2134–2156, 2011.

[15] A. Lion. A constitutive model for carbon black filled rubber: Experimental investigations and mathematical representation. *Continuum Mech. Thermodyn*, 8:156–169, 1996.

[16] Ju Liu, Marcos Latorre, and Alison L. Marsden. A continuum and computational framework for viscoelastodynamics: I. finite deformation linear models. *Computer Methods in Applied Mechanics and Engineering*, 385:114059, 2021.

[17] J. Lubliner. A model of rubber viscoelasticity. *Mechanics Research Communications*, 12(2):93–99, 1985.

[18] Christian Miehe and Serdar Göktepe. A micro–macro approach to rubber-like materials. part ii: The micro-sphere model of finite rubber viscoelasticity. *Journal of the Mechanics and Physics of Solids*, 53(10):2231–2258, 2005.

[19] Christian Miehe and Joachim Keck. Superimposed finite elastic–viscoelastic–plastoelastic stress response with damage in filled rubbery polymers. experiments, modelling and algorithmic implementation. *Journal of the Mechanics and Physics of Solids*, 48(2):323–365, 2000.

[20] B. Nedjar. Frameworks for finite strain viscoelastic-plasticity based on multiplicative decompositions. part i: Continuum formulations. *Computer Methods in Applied Mechanics and Engineering*, 191(15):1541–1562, 2002.

[21] B. Nedjar. Frameworks for finite strain viscoelastic-plasticity based on multiplicative decompositions. part ii: Computational aspects. *Computer Methods in Applied Mechanics and Engineering*, 191(15):1563–1593, 2002.

[22] Torben Netz and Stefan Hartmann. A monolithic finite element approach using high-order schemes in time and space applied to finite strain thermo-viscoelasticity. *Computers & Mathematics with Applications*, 70(7):1457–1480, 2015. High-Order Finite Element and Isogeometric Methods.

[23] M. Ortiz and L. Stainier. The variational formulation of viscoplastic constitutive updates. *Computer Methods in Applied Mechanics and Engineering*, 171(3):419–444, 1999.

[24] S. Reese and S. Govindjee. A theory of finite viscoelasticity and numerical aspects. *International Journal of Solids and Structures*, 35:3455–3482, 1998.

[25] Mark Schiebl and Peter Betsch. Structure-preserving space-time discretization of large-strain thermo-viscoelasticity in the framework of generic. *International Journal for Numerical Methods in Engineering*, 122(14):3448–3488, 2021.

[26] J.C. Simo. On a fully three-dimensional finite-strain viscoelastic damage model: Formulation and computational aspects. *Computer Methods in Applied Mechanics and Engineering*, 60(2):153–173, 1987.